ABSTRACT

STAMPS, MICHAEL ANTHONY. Mixed Modes Fracture and Fatigue Evaluation for Lithium Iron Phosphate Batteries. (Under the direction of Dr. Hsiao-Ying Shadow Huang.)

Lithium ion batteries have become a widely known commodity for satisfying the world's mobile energy storage needs. But these needs are becoming increasingly important, especially in the transportation industry, as concern for rising oil prices and environmental impact from fossil fuels are pushing for deployment of more electric vehicles (EV) or plug in hybrid-electric vehicles (PHEV) and renewable energy sources. The objective of this research is to obtain a fundamental understanding of degradation mechanisms and rate-capacity loss in lithium-ion batteries through fracture mechanics and fatigue analysis approaches. In this study we follow empirical observations that mechanical stresses accumulate on electrode materials during the cycling process. Crack induced fracturing will then follow in the material which electrical contact surface area is degraded and over capacitance of the battery reduces. A fatigue analysis simulation is applied using ANSYS finite element software coupled with analytical models to alleviate these parameters that play the most pivotal roles in affecting the rate-capacity and cycle life of the lithium-ion battery. Our results have potential to provide new models and simulation tools for clarifying the interplay of structure mechanics and electrochemistry while offering an increased understanding of fatigue degradation mechanisms in rechargeable battery materials. These models can aid manufacturers in the optimization of battery materials to ensure longer electrochemical cycling life with high-rate capacity for improved consumer electronics, electric vehicles, and many other military or space applications.

Mixed Modes Fracture and Fatigue Evaluation for Lithium Iron Phosphate Batteries

by
Michael Anthony Stamps

A thesis submitted to the Graduate Faculty of
North Carolina State University
in partial fulfillment of the
requirements for the degree of
Master of Science

Mechanical Engineering

Raleigh, North Carolina

2012

APPROVED BY:

_____	_____
Dr. Hsiao-Ying Shadow Huang Committee Chair	Dr. Jeffery Eischen
_____	
Dr. Gracious Ngaile	

DEDICATION

To my Parents, Jim and Janet Stamps. None of this would be possible without you.

My brother, Jimmy

My sister, Sam

Thanks for always being there.

BK and Punk as well

BIOGRAPHY

Michael Anthony Stamps was born in Tampa, FL in 1986. He attended Jesuit High School in Tampa, FL where he had an active lifestyle playing baseball, football, golf and lacrosse. He had always loved the outdoors and fishing, but was at the same time intrigued by aircraft and space exploration. This led him to pursue an engineering degree at the University of Florida where he was awarded a B.S. in Aerospace Engineering in 2010. It must also be noted that in his time at UF included two basketball national championships and two BCS football national championships within three year period while attending school with the face of college football, Tim Tebow. After Michael graduated, he held a position in the Navy department of Leslie Controls Inc. (Tampa, FL) designing flow control values for CVN-78, the new class of aircraft carriers. He then decided to take on graduate school in 2011 at North Carolina State University (Raleigh, NC) for pursuing a Master's degree in Mechanical Engineering. His field of interest and specialty is failure mechanisms, fracture mechanics, and modeling computer aided stress simulations for lithium ion batteries.

ACKNOWLEDGMENTS

I would like to thank NC State University and the Department of Aerospace and Mechanical Engineering for granting me the opportunity to study at this beautiful school. This experience has greatly increased my engineering aptitude while introducing me to a great part of the country in North Caroline, which I now love.

I'd like to thank my lab mates, Chen-Kai Chiu Huang, Siyao Huang and Yixu Richard Wang for their support in helping mold ideas while in the lab or at Hibachi for lunch on Fridays. They always showed a willingness to always take a minute to talk over an idea or question at all hours of the day.

To my roommates I've had over the years: Jesse, Tyler, Ben, Sam, and Ross. It was nice to have motivated friends who were always up for the adventurous ideas and trips on our free time. It was even nice to see you guys looking beat after a long day at work. It made me feel a lot better to know I'm still living the good life in graduate school.

I'd also like to thanks my committee members, Dr. Gracious Ngaile and Dr. Jeffrey Eischen for their priceless input for my project and willingness to always answer questions out of class. I always felt a little smarter after talking with my professors, for there weren't many one word answers, in fact you may come out having learned a lot more than you bargained for.

Finally, I'd like to thank my advisor, Dr. Hsiao-Ying Shadow Huang, for her second to none guidance and diligence for inspiring my thoughts and making sure I'm always progressing towards my goals. Thank you!

TABLE OF CONTENTS

LIST OF TABLES

Chapter 1

Chapter 2

Chapter 3

LIST OF FIGURES

Chapter 1

Chapter 2

Chapter 13

Chapter 4

CHAPTER 1 INTRODUCTION

The battery has long been a very important commodity for satisfying the world's mobile energy storage needs. But more than ever before, advanced lithium ion batteries are providing an increased level of interest due to expanded power capabilities and near limitless assortment of application opportunities. This research is driven to provide insight into the nano scale fracture mechanisms within the cathode material by accomplishing the following objectives to help aide in the understanding and development of a longer lasting, more power battery for the future. (1) Design a simulation to evaluate fracture mechanisms inside a single $LiFePO_4$ particle due to the lattice misfit phase transformation while cycling the battery; (2) create an energy based approach fatigue life estimation for $LiFePO_4$; and finally (3) identify what factors play the biggest role in inducing fracture while cycling and provide insight into what factors can be optimized to minimize any detrimental capacity loss in the battery. But first, chapters 1 and 2 will provide background information and related research in literature in order to understand the basic importance of lithium ion batteries along with their kinetics, strengths and limitations.

1.1 Lithium Ion Batteries

The advantages of lithium-ion batteries over other types or rechargeable batteries such as Nickel-Cadmium and Metal Hydride types lie in their superior energy-to-weight ratio, quicker recharge times, and increased cycle life [1]**.** It should also be noted that Co is

toxic and Ni may pollute as well, but $LiFePO_4$ is a nontoxic and environmentally benign material.

The lithium-ion battery is composed of three parts: the anode, an electrolyte solvent and the cathode which holds all the active lithium before operation. To charge, an external power source applies an over-voltage, forcing the active Li-ions from the cathode to the anode. When discharging, electrons flow out from the anode through an external wire to form an electrical circuit while Li-ions flow through the electrolyte to the cathode, thus neutralizing the charge (Fig. 1) [2]. The electrons provide electrical energy to any connected device until the lithium ion extraction and insertion processes are complete.

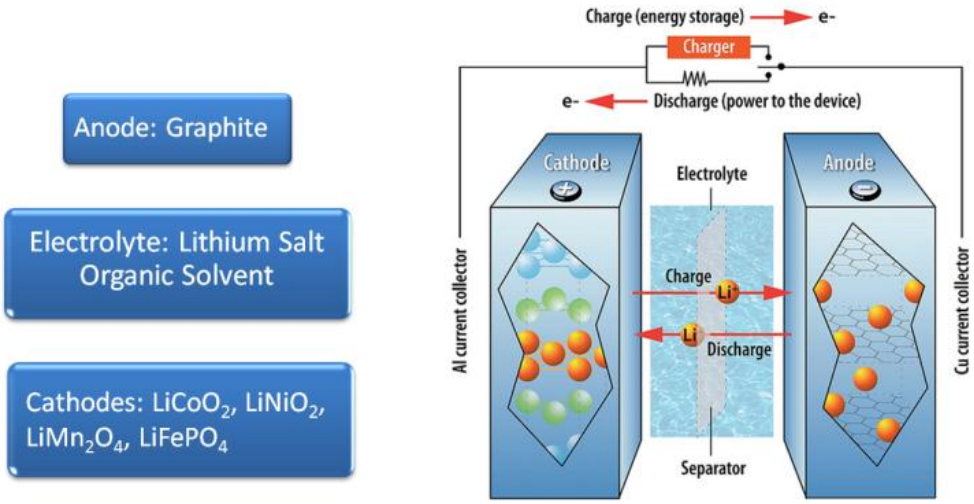

Figure 1. Lithium ion battery operation diagram. Li-ions travel back and forth between electrodes depending on charging state while electrons pass through an external circuit in the same direction to neutralize the charge and give power to a device [5].

A multitude of materials can be implemented for each battery component but anodes usually consist of a layered carbon structure, silicon nano wires, or titanate material whereas cathodes most commonly utilize an intercalated lithium compound such as $LiFePO_4$, $LiMn_2O_4$ or $LiCoO_2$ [3, 4]. A common electrolyte solution consists of an organic solvent containing lithium salt.

Batteries are now seeing performance increases that allow for high power application in electric vehicles, orbiting satellites and power tools in addition to everyday electronics such as and laptop computers and cell phones. But when we look closer at our world as it is today, it's evident that a battery's environmental impact and durability characteristic against climate variation are becoming very important in the material selection and design as well. Many different types of cathode materials are used to outfit today's electronic devices, each with its set of pros and cons. $LiCoO_2$, for instance, is popular in small, consumer electronics as it offers excellent power, energy density and charging/discharging capabilities. But this material lacks thermal stability, which raises concern for safety sensitive applications such as EV, HEV and PHEV. $LiMn_2O_4$ offers better thermal stability making it a possible choice for electric vehicles, yet it lacks the excellent power and energy density of $LiCoO_2$ [6, 7]. A vast opportunity for growth and improvement of lithium ion technology is still available. Researchers from Universities, National Labs, the U.S. Military and even NASA are currently involved in research for testing and improving $LiFePO_4$ technology, especially for use in high power applications like hybrid electric vehicles and space travel. The following sections will access why storage devices (batteries) are so critical to our world's future and

then also provide insight into a few lithium ion research projects from national labs and the United States Military.

1.2 Energy and Oil Outlook

For decades, petroleum products have been the backbone for transportation in the U.S. and around the world. About 50% of petroleum consumption is dedicated to the transportation industry while the other 50% is comprised for electricity generation and industrial or residential use [8]. In addition, environmentalist and scientist alike have studied the negative effects of the enormous carbon emissions to our atmosphere. It has been reported that 98% of all carbon dioxide emissions, the main contributor, come from petroleum fuels [9]. This has induced the drive for 'going green' which has become a worldwide epidemic. Thus, need to reduce our carbon footprint, especially in the petroleum driven transportation sector, is changing the way we design for the future. Today's society has become heavily reliant on oil consumption for its day-to-day activities, and prices are predicted to keep rising at relatively constant rates (Fig. 2) [10]. This over-reliance on petroleum will only stymie the world in the future as oil reservoirs are drained and fuel prices skyrocket.

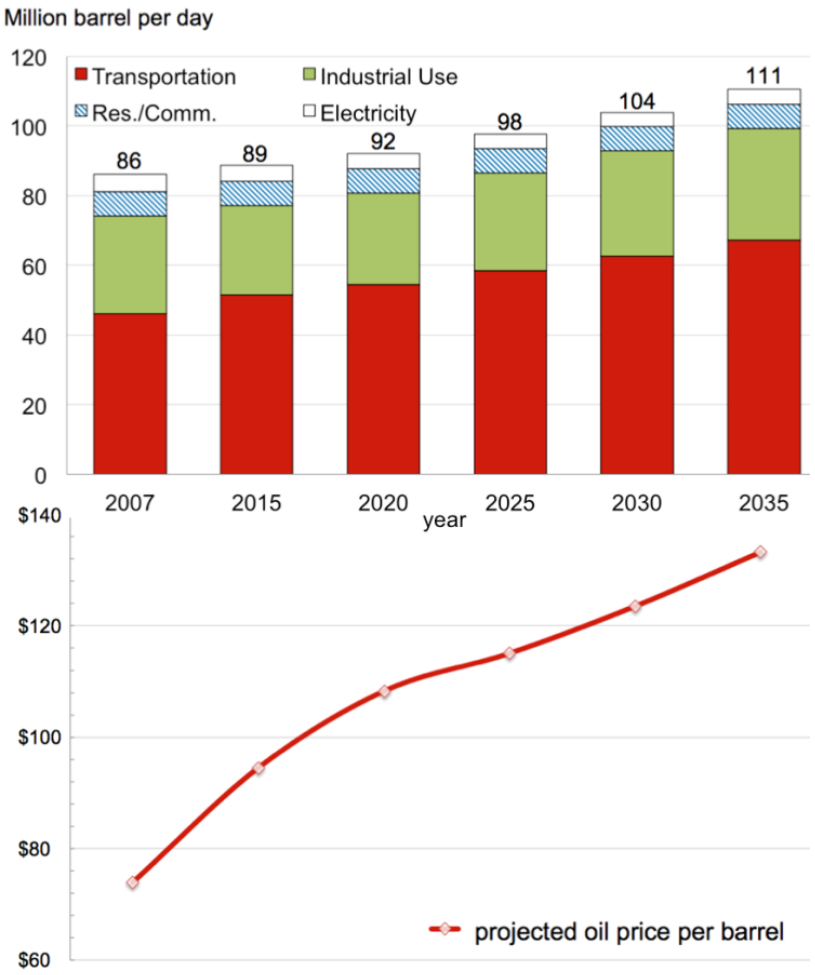

Figure 2. Oil Industry Trends. Current and future market trends in the oil industry for transportation, industrial use, residential and electricity generation. Trends show consistent increases in consumption and price through year 2035, but price increases at a slightly higher rate.

Not only is oil consumption around the world on the rise, but the demand for electricity is also increasing every year in our technologically driven world. Therefore, production must keep up with demand through the use of additional coal plants, nuclear plants, natural gas facilities and renewables such as wind, hydroelectric, biofuel, geothermal and solar energy among others. Renewables are by far the most attractive investment for the future as the energy source is essentially inexhaustible because it's naturally replenished. This includes wind, solar, geothermal, biofuels, wood, and hydroelectric power among others. In 2010, about 80% of electricity generation was obtained from fossil fuels (coal, natural gas, petroleum) while nuclear and renewables contributed about 10.0% each [11]. Thru the month of December during 2011, U.S. Energy Information Administration (EIA) reports that petroleum products, nuclear and renewables each contributed 77.6%, 11.3%, and 11.0% of U.S. energy production, respectively [10]. This growth trend is showing how large-scale energy production from coal plants is starting to fade in favor of the greener natural gas and renewable sources in the United States. Worldwide projections of electricity generation trends also depict great strides in areas such as natural gas and renewables as well (Fig. 3) [10]. Dozens of facilities across the world have recently taken advantage of technology advances by outfitting their facilities with large-scale batteries as backup or primary energy storage devices. Some of these locations include China (10 and 36 MWh facilities), the West Virginia Laurel Mountain wind farm (32 MWh facility) and Oahu, Hawaii (10 MWh wind farm). This data suggests there is a growing need for battery storage devices as a bridge between power generation and consumption more than ever before.

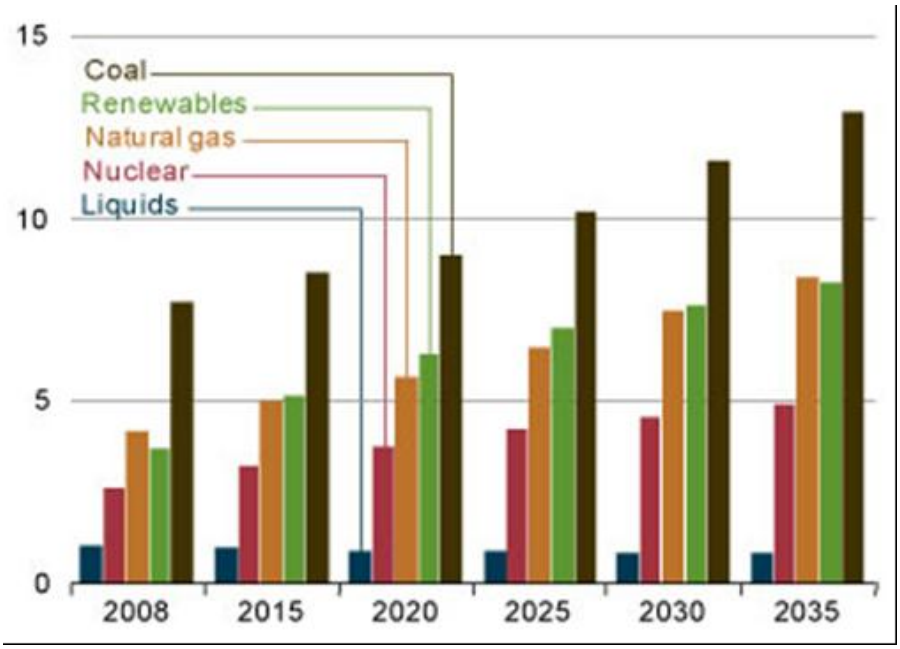

Figure 3. World net electricity generation by type. Natural gas and renewables are currently experiencing increased growth, especially with new wind, biofuel and solar power contributions [10].

1.3 Electric and Hybrid Vehicle Footprint

To help reduce our reliance on oil, U.S. Government policy has recently set requirements for auto manufactures by year 2016 in which an average of 35.5 mpg and a maximum CO_2 exhaust level of 250 grams per mile must be achieved for 'light vehicles' [2, 6]. This has helped increase research efforts in looking for alternative fuels and energy sources such as improved batteries for hybrid and electric vehicle transportation in particular.

Zero emission electric vehicle (EV) and minimal emission plug-in hybrid electric vehicles (PHEV) are already being manufactured and sold but lack in mass appeal due to

limited range and power. Lithium-ion batteries offer great promise for increased power, range and safety for vehicles, but improvements can still be made to increase cycle life, appeal and competitiveness in the automobile market. Figure 4 shows the current advantage of EV and PHEV vehicles regarding price and harmful emissions as compared to their gas counterpart of similar size and weight class.

Considerable economic and environmental saving advantages are evident for electrically powered vehicles, especially for zero emission EV's which are still considered by many to be in its 'infant' stage of technological design.

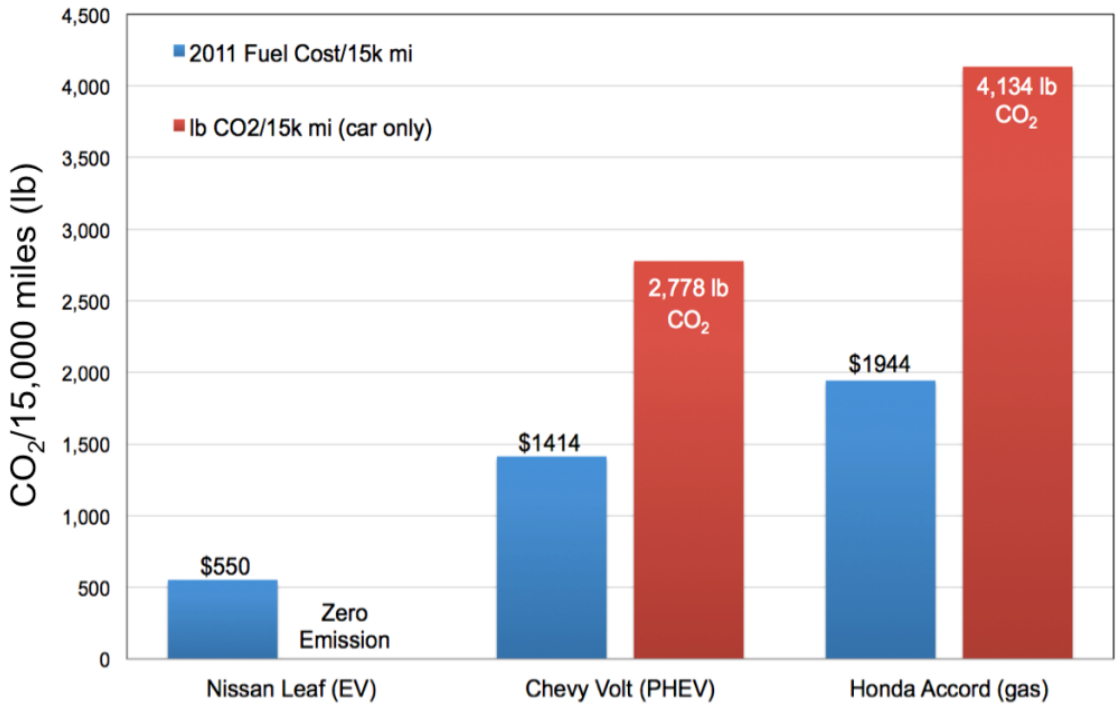

Figure 4. EV, PHEV and gas vehicle comparison. Vehicle operation cost and emissions per 15,000 miles. Gas price is estimated at $3.60 per gallon, electricity rate is averaged for 70% night charge and 30% day charging.

1.4 Government Funded National Labs

National labs, the Department of Energy, NASA and all facets of the military are very active in developing lithium ion battery technology for today's electronic driven world. The Army, Navy, Air Force and Marine forces rely on a multitude of battery driven devices and vehicles for day to day operation. Products include electronic sites on weaponry, night vision goggles, GPS units, small unmanned aerial vehicles (UAV) and mobile satellite radios. The Department of Energy invests millions of dollars every year on funding for attractive battery development research, especially EV and HEV related studies. The following describes several lithium ion research projects at national labs and government agencies in the effort to meet and exceed performance and safety demands for today and into the future (Table 1).

Table 1. Several Li-ion projects amongst National Labs, NASA, and the US Military.

	Material	Application	Focus	Findings	Comments
Argonne NL	$LiNiCoMnO_2$	HEV, PHEV	Develop high power, thermally and structurally stable cathode	Highest power ever reported for Li-ion battery, shows good safety, light weight	4.3–4.4 volts w/ high capacity > 210 mAh/g (50-100% increase over other mat'l at this time)
Sandia NL	$LiCoO_2$, SnO_2 (nanowire anode)	Potential for high power/energy density application	Tiny nano-size electrodes to understand Li-ion batteries from bottom up	Longitudinal swelling doubled wire length, diameter swelling much smaller	Results show nano wires as good electrode candidates. Can handle large stresses (>10 Gpa)
Pacific NW NL	$LiFePO_4$, $LiMn_2O_4$, $LiNiCoAlO_2$, $LiNiCoMnO_2$, $Li_4Ti_5O_{12}$	Stationary Energy Storage (solar/wind etc.)	Study various anode/cathode combinations	Cost Analysis (safety considerations included) in progress	Data will provide guidance in selecting best cathode option. Results TBD
Lawrence Berkeley NL	Sn/Carbon-nanocomposite	HEV, High power, high energy density applications	Fabricate graphene/Sn-nanopillar multilayered nanostructures (anodes). Prevent deterioration during cycling	High reversible Li storage capacity, good rate performance, high capacitance decay	Best Sn/graphene performance to date with slower capacitance decay than ever before
Oak Ridge NL	$LiCoO_2$ $LiFePO_4$	Design Optimization for all Li- ion batteries	Nanoscale mapping of Li-ion diffusion	Developed "electrochemical strain microscopy" to map Li-ion flow	Detail exceeds traditional electrochemical techniques by 6-7 orders of magnitude

	Material	Application	Focus	Findings	Comments
NASA	$LiFePO_4$ $LiCoO_2$ LiNiCoAlO2 LiNiMnCo	Landers, Rovers, Space Suits, Satellites, Solar Sails, Camcorders	Battery performance for space flight conditions (Thermal Stability, Capacitance, Cycle Life)	Li-ion has wide operating temps, Rapid recharge in smaller packs possibility	Weight and safety top priority. Li-ion lighter than current Ag/Zn. $LiFePO_4$ is thermally safest cathode
Military	LiNiCoAlO + more	UAV, Subs, Optics, GPS, Radios	High power and long life for Land, Sea, and Air Operations	Classified	N/A

1.4.1 Argonne National Lab

Researchers in Argonne National Laboratory's lithium-ion battery program (Illinois) have been focused on developing a high power, thermally and structurally stable cathode, $LiNiCoMnO_2$, for HEV and PHEV applications. The new material demonstrates resistance to overheating during high rate cycling, 5-kilowatt cold cranking at -30^oC, light weight, low cost and the highest power ever recorded for a manganese spinel based cathode material. The actual capacity is about 210 mAh/g, an increase of 50-100% over conventional materials. This material also shows the capability of meeting the energy requirements of supporting an electric-only trip of 40 miles [12].

1.4.2 Sandia National Lab

Application of high energy density tin nano-wires also shows some promise for reversible lithium ion battery technology. At Sandia National Laboratory, one focus is on tiny, nano-size electrodes to understand Li-ion batteries from a bottom up perspective is initiated with a $LiCoO_2$ cathode and SnO_2 anode combination. Reasoning for SnO_2 selection is due to the ultra-high power density and a specific capacity of over 900 mAh/g, though drawbacks include low electronic conductivity and high capacitance fading caused by large volume misfit from lithium insertion or extraction.

Tests show the nanowire anode allows for ultra-fast charging rates due to minute diffusion length and improved electron transport when a carbon coating or phosphorous doping is applied. TEM observation also showed that no fracturing in the coated material,

even with the 300% volume expansion. These results show great promise for phosphorous or carbon coated tin nanowire for the future [13].

1.4.3 Pacific Northwest National Lab

At Pacific Northwest National Lab, researchers are studying various anode/cathode combinations including $LiFePO_4$, $LiMn_2O_4$, $LiNiCoAlO_2$, $LiNiCoMnO_2$ and $Li_4Ti_5O_{12,}$ to compare viability for stationary applications such as solar, wind and load leveling applications. A cost and performance analysis including price per kWh, entropy change over 0-100% state of charge and rate cycling of half and full cells are conducted. Data shows that a LiFePo4/Li4Ti5O12 cathode/anode combination may show higher cost per kilowatt hour, but an impressive life cycle cost and stability for safety concerns is expected to make this combination very attractive over other possible pairs of electrodes [14].

1.4.4 Lawrence Berkeley National Lab

Berkeley lab researchers have fabricated multilayered graphene/Sn nanopillar composite structures for use as battery electrodes in super-high capacity, renewable lithium ion batteries. The nano pillar geometry reduces required lithium diffusion lengths while the sandwich structure provides freedom for the excessive volumetric changes during lithiation. This alleviates induced stress and strain and allows for faster charging with little or no

physical degradation while cycling. Although the material still experiences high capacity fade, improvements due to the sandwich structure showed high capacity retention of 98% and 93% after 15 and 30 cycles, respectively. This favorable result, along with high power performance due to a theoretical specific capacity of 992 mAh/g and high operating voltage show promise for further research to continue [15].

1.4.5 Oak Ridge National Lab

Researchers have developed a scanning probe microscopy method called ESM (electrochemical strain microscopy) for investigating lithium ion transport in layered electrode structures. This 'lithium ion mapping' method allows researchers to study the complex effect of interplay between ionic flow, material properties, microstructure and internal defects. The detail exceeds traditional electrochemical techniques by 6-7 orders of magnitude and will inevitably help in optimizing device parameters to reach the goal of building a better lithium ion battery [16].

1.5 NASA

1.5.1 Glenn Research Center

In 1997, The NASA Glenn Research Center conducted research to evaluate the performance of lithium iron phosphate batteries as a primary power source during lunar

extravehicular activities (space suit walks). The Portable Life Support System for a new advanced lunar surface space suit will be worn by astronauts during 8 hour long missions; therefore a lightweight power option is a goal. The missions also require that the power source have a long shelf life, operate in environments that differ from Low Earth Orbit (~900 mi altitude) to Geosynchronous (~22,000 mi altitude) applications, have a high specific energy and energy density, wide operating temperature, low discharge rate, and rapid recharge capability (Table 2) [17]. The current battery configuration is based on a Silver-Zinc cathode weighing in at 15 lbs with a 8 hour life. NASA chose to test the A123 M1 26650 lithium iron phosphate battery that exhibited excellent recharge rate capability, however, its specific energy and energy density is lower than typical lithium-ion cell chemistries.

Performance needs set goals to: develop a general performance characterization database for Li-ion cells (voltage response, current and temperature capability, impedance), quantify the ability of Li-ion cells to meet projected requirements, perform mission profile testing on cells and determine gaps in the ability of current technology to meet future needs so research investments may be focused.

The study compares an 8 hour case and 4 hour rapid recharge case to power an advanced space suit. The battery could only recharge for 15-30 minutes and the end of life was designated as the point when less than 80% of initial battery capacity is available for delivery after recharging.

Initial performance tests determined cell capacity and voltage response at different charge rates, discharge rates, and temperatures. Results were used to size a battery on paper and predict the mass and volume of battery required for the mission. Scaled mission profiles

run on single cells to verify performance (tests to determine if minimum voltage requirements are met). Results were analyzed and additional tests performed after adjustments were made.

Table 2. A123 Inc $LiFePO_4$ Cell Performance and Specs. [17].

Nameplate Capacity	2.3 Ah
Cell mass	72 grams
Cell Volume	0.035 liters
Nominal Voltage (C/2)	3.3 volts
Voltage Range	3.6 to 2 volts
Operating Temp. Range	-30 to 60 degrees C
Geometry	Cylindrical

The first performance test analyzed the Voltage vs Capacity for temperatures of 20 ^{o} C and -20^{o} C for different discharge rates from 10C to C/10 (e.g. 1C rate means the discharge current will discharge the entire battery in 1 hour. 10C rate discharges in 6 minutes (10x faster), C/10 rate discharges in 10 hours). The battery was initially charge at C/2 to 3.6 V for each different temperature. The battery showed good results for the warmer 20^{o} C temperature but inadequate performance at -20 ^{o} C for discharge rates faster than C/2. A Voltage vs. Capacity graph at C/2 shows that voltage and capacitance are held readily well

for temperatures above 20^{o} C (about 2.25 Ah at 2V), but a drop off is seen at 0^{o} C (2.16 Ah at 2V) and this rate of decrease accelerates as the temperature drops to -20^{o} C (1.77 Ah at 2V). These performance results show how this particular $LiFePO_4$ cell favored warmer environments in this study. Other tests conducted included "Charge Capacity at -20^{o} C for Different Rates", "Capacity Input at 4C Charge Rate" and "Voltage, Current and Temperature at 4C Charge Rate and 60^{o} C. It was concluded that the certain A123 cell tested is not optimized to operate on a full 8 hour discharge; reason being the $LiFePO_4$ cell tested contains lower specific energy than other Li-ion cells. But, in considering the 4 hour rapid recharge battery, operation at 20^{o} Celsius provides proficient energy and a 45% mass savings over an 8 hr Li-ion battery (Table 3). "Operational trade-offs must be performed to weigh the benefit of mass savings versus the added complexity of providing battery recharge capability in the field" [17]. Results show promise for a rechargeable $LiFePO_4$ space operations battery in the future.

Table 3. Battery sizing based on capacitance at -20 and 20 degrees C using C/10 discharge rate for 8 hour case and C/5 discharge rate for 4 hour case.

Temperature	20°C		-20°C	
Battery Version Used	8 Hour	4 hr + 15 min recharge	8 Hour	4 hr + 15 min recharge
Capacity avail. Per cell (Ah)	2.25	2.14	1.84	0.74
Nom. cell voltage (V)	3.29	3.28	3.19	3.12
# cells in series	6	6	6	6
# cells in parallel	18	10	22	27
Total # cells	108	60	132	162
Battery Mass (kg)	11	6	13	16
Battery Volume (liters)	11	6	14	17

Note: Recharge conditions were at 4C to 3.6V and voltage was held for 15 minutes before being terminated [17].

1.5.2 NASA Marshall Space Flight Center

NASA's Robotic Lunar Lander Development Project at the Marshall Space Flight Center has designed the next generation automated spacecraft "capable of exploring and conducting science on the surface of the moon, near-Earth asteroids, and other airless planetary bodies in the solar system" [18]. This new lander must have innovative on board battery systems that can withstand the extreme lunar thermal conditions ranging from 260^0 C in the day to -279^0 C at night. "Advanced, lightweight lithium iron phosphate batteries have proven themselves capable of supplying high power levels at sub-freezing temperatures, and permitting the team to devote more mass to payload" [18]. This response was elicited after cycling and charging times were examined under extreme temperatures. These results confirm $LiFePO_4$ as a viable candidate for space applications that could benefit many space agencies all over the world. It is interesting to note how low temperature performance improved for $LiFePO_4$ cells between testing at Glenn Research Center in 2007 and Marshall Space Flight Center in 2011 as new and improved $LiFePO_4$ batteries were used.

CHAPTER 2 $LiFePO_4$, A GOOD CATHODE MATERIAL

2.1 $LiFePO_4$ Conception and Attractive Properties

In 1996, conception of $LiFePO_4$ as a possible cathode for today's Li-ion batteries came to life when Dr. J. B. Goodenough's research group from the University of Texas identified a lithium insertion compound with olivine crystal structure that can be used as the cathode for a lithium battery (Fig. 5) [19]. The discovery of $LiFePO_4$ for use as a cathode was originally fueled by the battery industries' need for a low cost, highly available cathode material that out performs other cathodes (e.g. $LiCoO_2$, $LiMn_2O_4$, $LiNiPO_4$) by merit of watt hours per dollar. This low cost per energy provided specification is deemed much more important than watt hours per gram weight in the case of large batteries used in mass production manufacturing for electric vehicle or a load-leveling system. Therefore, investigations began looking towards iron for a cheaper solution.

Dr. Goodenough's group plotted electrochemical charge and discharge curves during their study and found that approximately 0.6 lithium atoms per unit formula were actually extracted from the compound at a closed circuit voltage of 3.5 V vs. lithium. The same amount could be inserted back into the structure on the discharge [19]. This reversible processes of lithium insertion into $FePO_4$ (heterosite) and lithium extraction from $LiFePO_4$ (triphylite) at 3.5 V vs. lithium at 0.05 mA/cm^2 affirm this material's ability to effectively perform as a battery electrode. $LiFePO_4$ and $FePO_4$ also show good thermal stability during

their fully charged state as seen by no change in weight at 350^{o} C and a 1.6% weight loss when heated to 500^{o} C in a nitrogen atmosphere.

After these initial findings, this material has regularly been a focal point for much experimentation and discussion as it boast several attractive qualities including a relatively high theoretical capacity of 170 mAh/g, great structure stability, long cycle life, environmentally benign qualities and most importantly, great thermal stability for safety (Table 4) [19].

Table 4. $LiFePO_4$ Cathode Specifications.

Nominal Voltage	3.3 volts
Temp Range	-20 to 60 degrees C
Cycle Durability	2,000 + Cycles
Capacity	90-130 $mAhg^{-1}$ (170 theoretical)

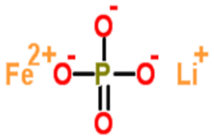

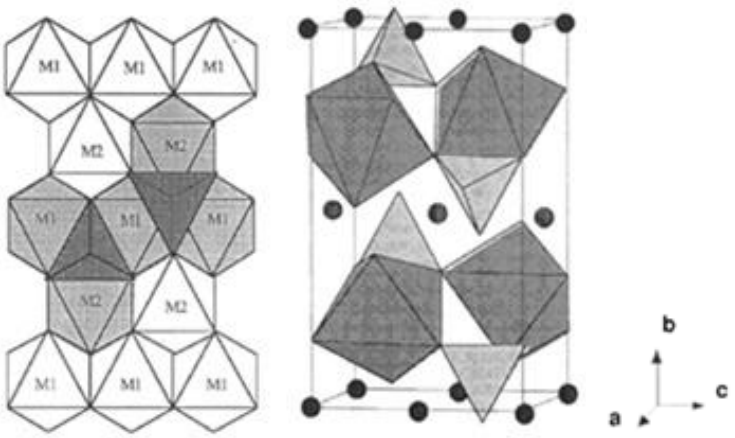

Figure 5. Olivine Crystal Structure. M1 represents lithium and M2 represents Fe [19].

The wide operating temperature range is very helpful for vastly changing environments or seasonal conditions while the long cycle life can provide enough long term power for applications in electric and hybrid electric vehicles. It is also important to note that the safe operating characteristics of $LiFePO_4$ are due to superior thermal and chemical stability. Thermal stability testing by use of differential scanning calorimetry testing can determine a material's ability to absorb or emit heat during an electrochemical reaction. This test is usually performed to investigate exothermic and endothermic reactions for composite explosives but can also be used for lithium insertion and extraction reactions. Test data shows decomposition temperatures of $LiCoO_2$, $LiMn_2O_4$ and $LiNiO_2$ at 340^oC, 275^oC and 250^oC, respectively. $LiNiO_2$ and $LiCoO_2$ also show significant exothermic reactions, unfavorable for vehicle application as overheating could very easily occur [20]. $LiFePO_4$, on the other hand, is endothermic, not releasing heat during the electrochemical reaction and decomposition doesn't take place until temperatures rise above 900^o C [21]. This material feature allows the cathode to withstand higher temperatures than other cathode materials and thus is currently the safest cathode material for vehicle and human sensitive applications.

2.2 $LiFePO_4$ Challenges

However, there are drawbacks to $LiFePO_4$. An early obstacle of $LiFePO_4$ was overcoming the extremely low electrochemical conductivity around 10^-9 S cm-1 in raw $LiFePO_4$, a quality that is essential for battery design. But great strides have been achieved in improving this conductivity by means of applying conductive carbon coatings or cation

doping the surface [1, 22, 23]. Newer studies are interested in mitigating or even eliminating capacitance fading during cycling, a major design obstacle if lithium batteries are to be improved. Therefore, understanding degradation mechanisms involving internal stresses due to charging/discharging or lithium diffusion is of high priority to improve $LiFePO_4$ performance, and lithium ion batteries in general.

Another drawback may be a product of the two phase interface (Fig 6). Lithium insertion proceeds from the surface of the particle moving inward behind a two-phase interface; as lithium transport proceeds at a constant rate, the interface surface area between phases shrinks. Eventually, the interface surface area decreases to a critical point where diffusion through the interface cannot keep up with the volume of lithium provided. Cell performance, therefore, becomes diffusion limited [24].

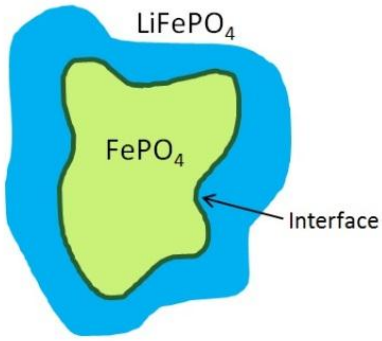

Figure 6. Schematic representing $LiFePO_4/FePO_4$ 2-phase interface during charging or discharging.

2.3 Electronic Conductivity Improvements

For the past two decades, scientists and engineers alike have tried to improve the electric conductivity and electrochemical properties of $LiFePO_4$ by several means. Among the methods conducted, carbon coating of around 10nm was, and still is, considered an easy and effective way to get better electric conductivity and electrochemical properties [25]. But successful improvements to the carbon doping process and additional electrochemical coating processes have also been developed over the years.

2.3.1 Supervalent Cation Doping

Carbon doping and co-synthesizing have been shown to increase electronic conductivity for $LiFePO_4$, but these processes pose drawbacks such as a need for additional processing and a loss in energy density due to the electrochemically inert additive [1]. Dr. Chung offers a method he calls 'selective doping with supervalent cations' to increase the lattice electronic conductivity by a factor of 10^8 to reach values greater than 10^{-2} S cm^{-1} at room temperature. This is a large increase over current storage cathodes, $LiCoO_2$ and $LiMn_2O_4$, which only provide ~10^{-3} S cm^{-1}, and 2 x 10^{-5} to 5 x 10^{-5} S cm^{-1}, respectively. The results of such a process increases performance to near-theoretical energy density at low charge/discharge rates and shows significant capacity retention with low polarization at rates as high as 6,000 mA/g [1].

Maintaining high electric conductivity in a typical battery electrode is imperative for preventing the impedance from becoming overly excessive. It was seen that utilizing low doping levels to increase conductivity did not decrease storage capacity at low rates, but did in fact increase the power density. “The decreasing capacity with increasing current rate is most probably due to limited lithium diffusion.” Selective doping with supervalent cations shows positive results for increasing electric conductivity of the cathode material as described above. The reason behind this effect lies in the study of the doping and defect mechanisms in the material.

2.3.2 Polythiophene Coatings

Polythiophene (PTh) coatings provide another method to improve electrical conductivity of the $LiFePO_4$ cathode [22]. Dr. Bai reports testing on $LiFePO_4$/PTh cathode material samples prepared with 5.86 wt. %, 10.56 wt. % and 12.85 wt. % PTh coating that were visually inspected by TEM. When the coating weight percent reached 10.56 %, the particle surface was completely and uniformly coated with PTh whereas the 12 wt. % sample showed a thickening of the surface. A Nyquist plot of bare $LiFePO_4$ and $LiFePO_4$/PTh was created and parameters of the equivalent circuit (Table 5) were obtained from pc simulations using Zview2.0 software.

Table 5. Electronic conductivity of bare $LiFePO_4$ and PTh coated $LiFePO_4$. The data suggest there is tradeoff between increasing conductivity and lowering specific capacity and energy density, as determined by wt. % PTh. Resistance (R_s), charge transfer resistance (R_{ct}), and current density (i_o).

Sample	R_s (Ω)	R_{ct} (Ω)	i_o (mA)
Bare $LiFePO_4$	3.29	280.2	0.09
5.86 wt% $LiFePO_4$/PTh	4.54	84.76	0.298
10.56 wt% $LiFePO_4$/PTh	4.06	50.92	0.496
12.85wt% $LiFePO_4$/PTh	3.97	64.12	0.394

The transfer resistance (R_{ct}) of the $LiFePO_4$/PTh composites was smaller while the current density was larger than bare $LiFePO_4$. This indicates improved electronic contacts between $LiFePO_4$ particles due to the PTh coating and improved overall performance of the battery. A voltage versus capacity plot under constant current density rate confirms this statement.

"The polythiophene has a practical capacity of 49.98 $mAhg^{-1}$ at the C/5, which is much lower than that of $LiFePO_4$ with its theoretical value of 170 $mAhg^{-1}$. So increasing the PTh in the composite would reduce the specific capacity of the composite's electrode. However, an increase in PTh would also improve the electric conductivity of the composites and increase the utilization of $LiFePO_4$, inducing an enhanced specific capacity." Therefore, a compromise is present when considering the amount of polythiophene used [22].

Collectively, testing indicates that $LiFePO_4$ with 10.56 wt. % PTh coating may be a reasonable choice for this type of cathode material.

Discovering ways to increase the electronic conductivity has secured the label of $LiFePO_4$ as a good cathode material. This has allowed research to direct the focus on other areas needing performance enhancement so one day we may achieve theoretical while eliminating capacitance fade over time

2.4 Phase Boundary Orientation

In the past, a popular avenue of theoretical thought has attributed rate capability of olivines like $LiFePO_4$ purely to chemical diffusion limitations. But as these olivines undergo a first order phase transformation, an equally important analysis may be to access "whether the phase transformations kinetics, which corresponds directly to the rate of lithium exchange, may be affected by other, structural factors" [26]. To put this idea to the test, several researchers have completed studies on $LiFePO_4$ regarding lithium movement, lattice misfit and particle geometry during the phase transformation process.

The phase transition occurs during charging/discharging in which the triphylite ($LiFePO_4$) is transform into heterosite ($FePO_4$) as Lithium ions are transferred from cathode to anode and vice versa. A previously stated "shrinking core model" was the widely accepted mechanism during this phase transformation process. But as recently as 1996, Chen, Song, and Richardson utilized TEM and SEM observations in their research to challenge this idea found that this shrinking core model does not apply to $LiFePO_4$. Their results show

movement of Li ions is strictly confined to tunnels along the b-axis or [010] direction of the particle (Fig. 7). This, coupled with the fact that Li motion through bulk solids is highly restricted, provides another idea that "rather than diffusing through the crystals, Li is extracted or inserted only at the phase boundary, with Li ions moving in a direction parallel to the boundary" [26]. The b-c plane is the leading candidate of the phase boundary orientation due to the preference of diffusion along this direction and the bonding weakness between the b-c layers. "This has already been confirmed for $LiMnPO_4$" [23].

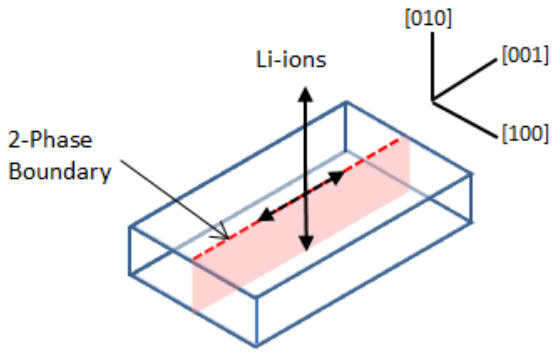

Figure 7. Illustration of the phase transition zone and favored

2.4.1 Dislocations and Cracks Alignment

During TEM and SEM observations, features of dislocations were located on oxidized crystals aligned with the bc plane and in the c axis direction. These dislocations were found to form or nucleate into an "extended phase boundary" along the face of the crystal along the c axis. Then bond stretching and twisting in the boundary phase occurs, which may allow the

Li molecules to have more freedom, increased mobility and conductivity versus that in a crystalline line phase. This nucleation phase provides insight into why $LiFePO_4$ charges at such a high potential. In general, it was noted that if there are enough initial nucleation sites (where the ac- faces and conducting matrix have ample connection) to support the required charging current, no other nucleation sites will form. Otherwise, less favorable sites with lower connectivity will stimulate nucleation. This will occur when a very rapid charging rate requires more Li-ions. Added stress will be introduced during these situations as well, increasing the disordered region and Li-ion mobility in the process. This insight into the movement and location of Li-ions causing dislocations and high stresses will help in pinpointing the prime areas relating to fracture and capacitance loss over the cycle life of the battery [26].

2.5 Misfit and Strain

In a Li-ion battery, both electrodes are atomic frameworks that host mobile lithium ions. As the battery is being charged or discharged, lithium ions diffuse from one electrode to the other in a process called intercalation or de-intercalation. This insertion reaction may deform the electrodes, resulting in cracks and fracturing which reduce the useful surface area for future insertion and degrades the battery's capacitance. Therefore it's important to understand this degradation mechanism, starting with stress modeling.

Extended lithium nonstoichiometry coupled with decreases misfit percent has been observed in both end member phases of high rate doped nanoscale lithium phosphates.

Examples of how strain affects misfit, which contributes to poor rate capability has been verified within $LiFePO_4$ itself and now may lead to answers to other questions such as why $LiMnPO_4$ has a much poorer rate capability than $LiFePO_4$ ($LiMnPO_4$ has a much higher misfit %) [27].This conclusion suggests that misfit, and inevitably strain distribution, plays an equally important role in rate capability as ionic and electronic transport. Strain based criterion, therefore, may need to play an important role in selecting the proper material for a high power battery compound.

2.6 Particle Sizing Effects

Discoveries involving improved performance of nanoscale olivines, such as described in the previous paragraphs, began producing results previously unpredicted from scaling laws. This raised the question, "are their fundamental changes in physical properties of these materials in the nanoscale regime?" [28]. In 2007, an X-Ray structural analysis and electrochemical test of lithium-iron phosphate powders were performed on three samples of the following average sizes: samples A and B had specific surface areas of 48.8 and 39.4 m^2/g with spherical diameters of 42 and 34 nm, respectively. Sample C was a commercially available carbon-added $LiFePO_4$ with a specific surface area of 14.8 m^2/g and 113 nm spherical particle diameter.

Galvanostatic charging and discharging measurements were performed to test the two-phase plateau voltages of the different sized particles. At the voltage plateau, capacity is seen to increase with decreasing particle size suggesting a shrinking miscibility gap with a smaller

particle size. At 50% SOC, it was also found that samples A and B have a higher retained strain than C. This increase in strain seems to be caused by a small amount of misfit in lattice parameters and unit cell volume between the triphylite and heterosite phases. Reasoning behind these particle size effects sprouts from a few possibilities as described by the authors: increases due to relative contribution of particle-matrix surface energy and surface stresses; coherency or compatibility stresses in two-phase particles with a coherent interface. “One possible explanation is the coherency stresses arise when the misfit between triophyte and heterosite phases in partially transformed particles is small enough to retain a coherent interface... As the misfit increases, as in sample C, incoherent interfaces are created that relieve the strains” [28].

In conclusion, a decrease in the miscibility gap was observed below about 100 nm particle diameter and as the particles became even smaller, an enhanced solubility was also observed. The coherency stresses are seen when a nucleation of a second phase of thriphylite or heterosite arouses from a currently single phase of the other. Since triphylite has a larger molar volume, it experiences compressive stresses while heterosite undergoes tension. This dominance of compressive stress will decrease Li solubility as seen by smaller and smaller particle sizes. It must be noted that other contributions to free energy not listed here could contribute including “antisite disorder or other lattice defects” [28].

2.6.1 Smaller Misfit with Smaller Diameter

Another study by Meethong tests two samples of lithium-iron phosphates, a commercially available carbon added and "battery grade" $LiFePO_4$ material denoted AC along with a recently synthesized, cation-doped $LiFePO_4$ denoted as NC. The NC sample had a specific surface areas and spherical particle diameter of 39.2 m^2g^{-1} and 43 nm. The AC sample was 14.8 m^2g^{-1} and 113 nm in diameter. Initially, it was though a correlation exists between decreasing lattice misfit with increasing nonstoichiometry. This correlation was confirmed in this study as sample AC contained about 6.63% volume misfit while NC contained approximately 4.15% volume misfit. These misfits contribute to the strains attained on each plane and therefore decide where the interface of coexisting phases will form (this will be the plane observing the minimum strain (the {100} or bc plane). Observations from prior research also shows that misfit, even along the plane with minimum strain, can cause rupture [27].

Incoherent interfaces are also causes for kinetic limitations. If a large enough lattice misfit is present, the interface should have a slower migration rate due to interface dislocations. These dislocations cannot migrate due to Li transport alone, as seen with coherent interfaces, so they must be removed by a climb and glide process that requires slow phase boundary movement for them to propagate to the particle surface. As seen in this study, a TEM of sample AC after 30 high rate charge/discharge cycles showed a high density for dislocations. But these defects were difficult to detect in the smaller diameter NC particles, which contained a smaller misfit percentage [27].

2.7 Theoretical Stress Modeling During Li-Diffusion

In 2010, Dr. Renganathan developed a mathematical model for the stress and strain accumulation in a $LiCoO_2$ cathode material that not only concentrates on a single particle, but supports the entire makeup of a porous electrode. This is a process that could possibly be altered to fit $LiFePO_4$ with the addition of anisotropic effects in the future.

Dr. Renganathan asserts that, "The objective of our study is to use a comprehensive mathematical model to (i) develop a correlation between the mechanical properties and performance of the porous battery electrodes and (ii) understand the importance of the structural and mechanical properties of the electrodes in determining the durability of the battery electrodes for a given set of operating conditions." To accomplish this, a model was developed to take into account "(i) diffusion into the intercalation electrode particles (solid phase), (ii) stress generation due to intercalation and phase transformation processes in the electrode particles, (iii) diffusion and migration in the electrolyte (solution phase), and (iv) electrochemical reaction at the solid/solution interface" [29].

The author's model uses spherical particles and take into account phase effects. Different phases will have their own mechanical properties, diffusion rates, and composition leading to different stresses at the phase interface. To track this process, the "Moving Boundary Model" presented by Zhang and White is used and diffusion equations for both the lithium rich and lithium poor phase are provided. To formulate the equations describing stress buildup in the particles during intercalation, assumptions are made: "(*i*) mechanical properties are assumed to be constant within each phase of the intercalation material, (*ii*) the

material is assumed to be completely elastic until failure, and (*iii*) mechanical equilibrium is assumed to exist within the material" [29].

It was found that stresses due to lattice volume changes (misfit) and phase transformation during intercalation are directly related to the state of charge (SOC) of the particle. SOC can be defined as the ratio of average lithium concentration at a certain time to the maximum possible concentration value. As stated earlier, the misfit stress is developed from a misfit strain at the phase boundary to maintain a coherent interface. This misfit strain is seen to give rise to a differential stress at the phase boundary with primary tangential component. It is reported that the distribution of the stress across the entire bulk electrode closely resembles the phase transformation in an individual particle.

"The intercalation stress increased with the rate of discharge, and the phase transformation stress depended on the amount of each phase present in the electrode. The results from the simulation indicate that the particles that are cycled over an extended period at intermediate or even low rates of discharge can be damaged due to the residual strain buildup caused by phase transformation in the material" [29].

2.8 Fracture Mechanics to Avert Cracks

Cracks caused by mismatch of phases in $LiFePO_4$ particles are considered in a simulation study to try and determine a critical particle size, below which cracking will not occur. The model was based on realistic geometry of $LiFePO_4$ particles including plate like and equiaxed or spherical shapes. "The insertion-induced deformation is often constrained by

mismatch between active and inactive materials, between grains of different crystalline orientations, and between phases of different concentrations of lithium. Under Such constraints, the insertion and extraction of lithium induces a field of stress in an electrode, which may cause the electrode to form cracks. Cracks may break off pieces of active material from the electrode, causing the capacity of the battery to fade" [30].

The authors analyzed stresses around cracks on the bc phase boundary for the plane stress condition as the particles were thin and plate-like. Thicker particles were also considered and the plane strain conditions were applied in this case. In previous experimental observations, "Cracks were found in plate like particles of dimensions 4x2x0.2 nm and cracks were also found in equiaxed particles of different particles of size 300-600 nm and 200 nm. When particle size was <30nm, no cracks were observed". $LiFePO_4$ is under compression near the phase boundary, but is under tension near the face of the particle, where the crack is taken to initiate [30].

A maximum energy release rate coefficient was calculated for many different crack sizes based off the material elastic modulus, misfit strain percent, surface energy and particle size. A simple mathematical expression was then used to obtain the critical value of 605 nm for plate-like particles and 58nm for equiaxed particles. "When the maximal energy release rate is below the critical value, no cracks in the particle can advance. "We hope that more experimental data will be made available to compare with the theoretical calculation" [30]. This approach would allow someone to compare strain energy release rate values to their data and determine if the particle would crack or not, a simulation that my personal research project has developed with ANSYS, an FEA software package.

2.9 Fracturing Caused by Stress and C-Rate

As the relationship between microscopic fractures and the 2-phase interface is currently unknown, experimentation in this area is very valuable to the efforts for advancing $LiFePO_4$ as a cathode material. Drs. Gabrisch, Wilcox and Doeff have examined and compared samples of $LiFePO_4$, one subjected to chemical delithiation and the other to electrochemical cycling. "We observe the formation of micro fractures parallel to low indexed lattice planes in both samples. The fracture surfaces are predominantly parallel to (100) planes in the chemically delithiated powder and (100) and (010) planes in the electrochemically cycled powder. A consideration of the dislocation stress fields shows that particle geometry plays an important role in the observed behavior" [25]. Plate-like particles were considered in this study.

Figure 8 shows the corresponding diffraction and TEM image for a hydrothermally prepared $LiFePO_4$ sample. When comparing the 2 samples, the most prominent feature seen in both is fracturing along planes parallel to low index lattice planes. "The number of fractures observed in the chemically delithiated material is considerably higher than in the electrochemically cycled powders, underlining the correlation between internal stresses and particle fracturing. The magnitude of misfit stresses in the system $LiFePO_4/FePO_4$ is expected to be highest at a lithium content $x = 0.5$; however, high lithium extraction rates, such as those used in chemical delithiation, add to the magnitude of internal stresses" [25]. As seen in Figure 9, dislocation density is much higher in the chemically delithiated particle than that of the cycled particle as well.

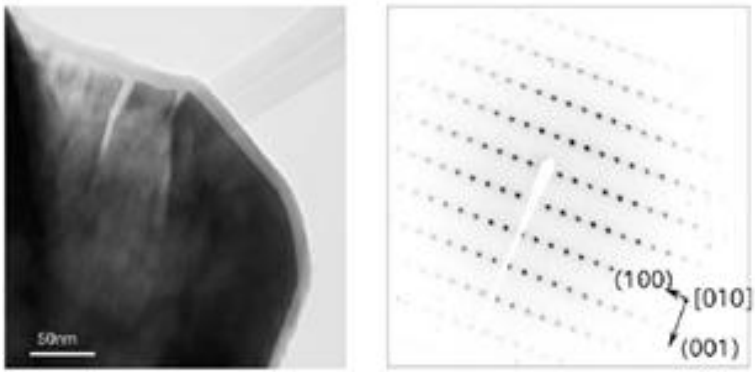

Figure 8. Image (left) and diffraction pattern (right) of LiFePO4. Fracture surface is oriented parallel to (100) planes. The diffraction pattern shows spot splitting, typical for a 2-phase microstructure [25].

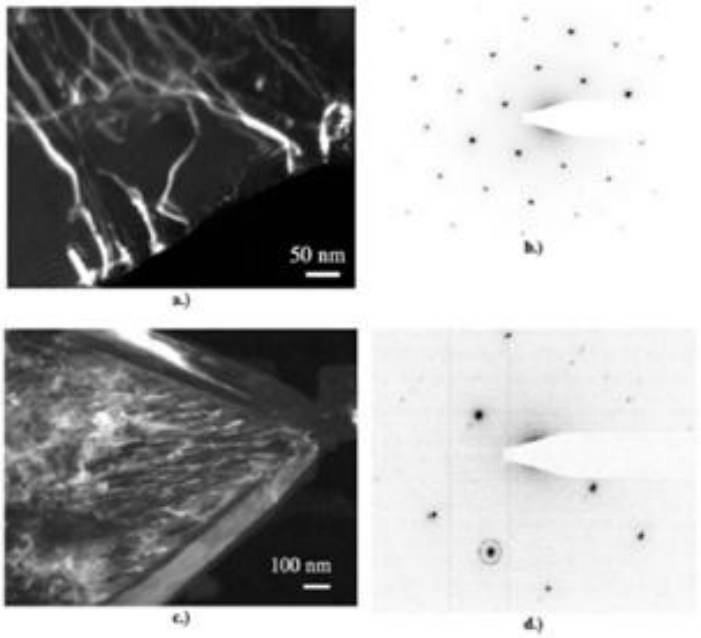

Figure 9. Dark-field images and diffractions patterns of a cycled LiFePO4 cell (a, b) and a chemically delithiated LiFePO4 particle (c, d) [25].

Through studying the olivine structure of $LiFePO_4$, trends on how bonds break can be seen between FeO_6 and PO_4 polyhedra. Thanks to Third Pauli's Rule, it is known that corner sharing bonds have higher stability than that an edge or face bond. Therefore, it's much easier to break the bonds on the (010) planes, thus the preferred direction of fracture is along these (010) planes. Elastic strains produced through dislocation formation in a crystalline material gives rise to stresses that are proportional to the Burgers vector, b, and the material's bulk modulus, G. For an isotropic material, it is known that elastic stress is the smallest for dislocations with the shortest Burger vectors. However, due to the orthogonal anisotropy of $LiFePO_4$, directionality bulk moduli and the length of the Burgers vectors need to be taken into account. The qualitative deviations between elastic stress fields from dislocations with 100 directional Burgers vectors in $LiFePO_4$ using anisotropic elastic moduli were calculated by use of first principles by Maxisch and Ceder (Table 6) [31].

Table 6. Bergers vector magnitude, directional Bulk Moduli (G), and their product. The [010] direction is favored for fracture.

Direction of Burgers vector (b)	Magnitube of b (10^{-10} m)	G (10^9 Pa)	G*b (N/m)
[100]	10.33	207	214
[010]	6.01	459	276
[001]	4.7	279	131

2.10 Fracture Caused by Fast Charging in $LiCoO_2$

As lithium ion batteries become increasingly popular for high power operations such as electric cars and scooters, special attention must be paid to elevated stresses that occur within the material when high discharge rates are applied. “If the battery is charged at a rate faster than lithium can homogenize in an active particle by diffusion, the inhomogeneous distribution of lithium results in stresses that may cause the particle to fracture” [24].

As previously known, migration of lithium in the electrolyte is very fast while the rate of lithium diffusion into the electrode is much slower, making diffusion a rate limiting process during a charge or discharge. The stress created by lithium insertion or extraction is often caused by mismatch stemming from the inhomogeneous distribution of lithium within the particles. The challenge of fast charging is analogous to a traffic jam during rush hour which can cause major backups, stress and problems as we see in our everyday lives.

The authors experiment helped to define a region of fracture vs. non fracture for $LiCoO_2$ molecules during charge/discharge. It was shown that crack damage was seen in particles of size 300-500 nm after 50 cycles and that cracks can be prevented by decreasing particle size and/or discharge rate. More data for different particle sizes and discharge rates is needed to further solidify the model [24].

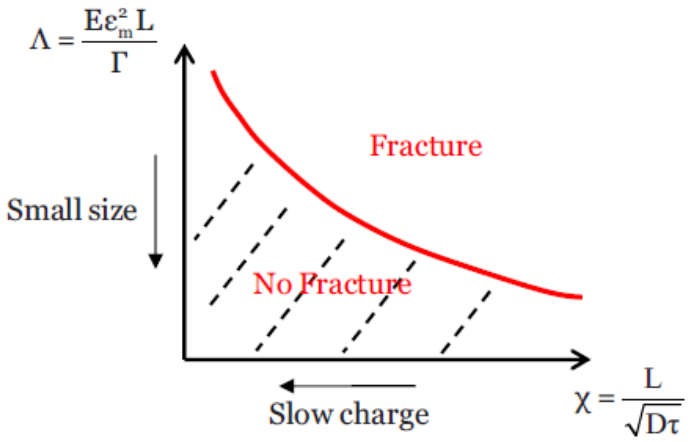

Figure 10. Criteria to avoid fracture of an electrode particle. Λ is a dimensionless coefficient defining the comparison between energy release rate fracture energy. X characterizes the discharging rate versus diffusion rate [24].

2.11 Electrochemical Shock

As mechanical fracture has been pointed out as a possible source for capacity fade and impedance growth in Li-ion batteries, research by Woodford presents a study to determine fracture failure criterion, which is necessary in order to design mechanically robust Li-ion cathodes with better performance and life-prolonging life cycles.

In this paper, diffusion-induced stress is calculated and LEFM is used to predict fracture for a brittle $LiMn_2O_4$ electrode material. Single particles with initial flaws are studied and stable or unstable crack conditions depending on stress intensity factors are estimated.

Crack faces are assumed to be electrochemically inert so only the outer particle surface is reactive; $LiMn_2O_4$ is treated as a continuous solid solution 0<=x<=1 with elastic plastic properties that are constant across the full composition range [32].

A two-step method will predict the K_i (stress intensity factor). First, diffusion induced stress is calculated over a range of galvanostatic, or constant current, charge rates. Then the stress profiles obtained at 'end of charging' (the most extreme loading condition) are used to predict K_i as a function of the particle flaw size. The pdepe solver function of MATLAB is used to numerically solve the problem made up of 17 equations.

A limitation to the technique described in this paper: "Diffusion-induced stresses in our model arise only from internal composition gradients, not from overall changes in composition. These results are directly applicable to single phase materials, where stresses arise from concentration gradients. Future modifications will include first-order phase transformations or interface coherency stresses" [32].

"In brittle materials, surface flaws subjected to tensile stresses are the most common origin of catastrophic failure. For this reason, we simulate charging (deintercalation) of Li$x$$Mn_2O_4$, which produces tensile tangential stresses because the partial molar volume of lithium in this material is positive and tend to open the surface flaws." Stress intensity factors are computed with the aid of the 'method of weight functions' and an edge-cracked plate with a uniform stress loading pattern. The Ki for the problem is as follows where K_{ref} is the reference stress intensity factor and $m(x,a)$ is the weight function (a kernel or Green's function) against which the diffusion-induced stress profile is integrated. The stress distribution $\sigma_\theta\ (x)$ is the tangential component of the diffusion-induced stress at the end of charge.

$$K_i = \frac{E}{K_{ref}(1-\nu^2)} \int_0^a \sigma_\theta(x) m(x,a) dx \quad [32] \tag{1}$$

2.11.1 Initial Flaw Size

Results show a shock map relating fracture to flaw size and charge rate (Fig. 11). The authors also conclude that it may be possible to charge rapidly without inducing fracture if one starts the charge at a low rate and subsequently increases the rate slowly. This may be possible because having low initial rate can build up a reservoir of composition in particle's center which may limit the maximum concentration gradient inside the particle so higher charge rates won't have as big an effect.

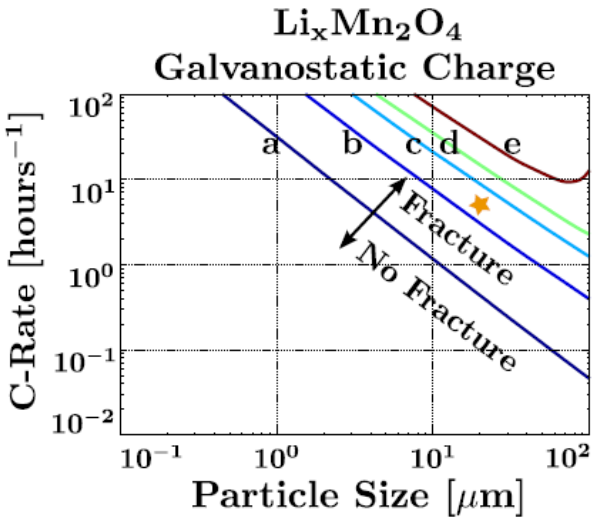

Figure 11. Electrochemical shock map. Curves represent on the set of fracture for five estimated values of fracture toughness (0.1, 1, 3, 5, 10 MPa*$m^{1/2}$) of $LiMn_2O_4$ [32].

The paper also provides evidence, matching Hasselman's classic result for thermal shock, where small initial flaws may be more damaging than larger flaws because the small flaws have a more detrimental effect on the strength of brittle materials as they grow unstably while large flaws will grow in a stable manner (Fig. 12) [32].

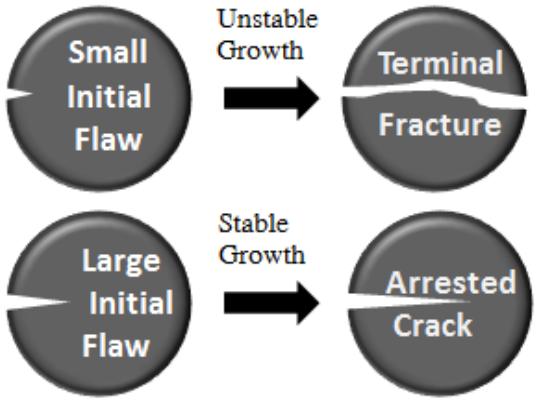

Figure 12. Unstable growth of small initial flaw as can lead to terminal failure of electrode particles. Relatively large initial flaws exhibit stable growth and the crack can arrest at a final length when K_I (arrest) = K_{IC}.

CHAPTER 3 MIXED MODE FRACTURE MECHANICS SIMULATIONS

3.1 $LiFePO_4$ Material Properties and Performance Characteristics

This chapter highlights the efforts to accomplish the first research objective of this work in the creation of a simulation to evaluate the fracture mechanisms inside a single $LiFePO_4$ particle.

$LiFePO_4$ is an anisotropic material with three different elastic moduli for each orthorhombic direction. E_{11}, E_{22}, and E_{33} apply to a=[100], b=[010], and c=[001] principal directions [31]. These values are obtained by use of ANSYS solving the elastic moduli equations (Equations 2-4) after inputting the specific directional elastic constants of the anisotropic-orthorhombic material (Table 7 and 8). Elastic constants (C_{ij}, $i = j = 1, \dots 6$) quantify the response of a material to an elastic, or reversible, deflection and thus are utilized to evaluate a material's elastic modus (Young's modulus). This a material dependent constant defining the stiffness of a material by measuring the ratio of stress in a body to the corresponding strain.

$$E_{11} = \frac{(c_{11}c_{22}c_{33}+2c_{23}c_{12}c_{13}-c_{11}{c_{23}}^2-c_{22}{c_{13}}^2-c_{33}{c_{12}}^2)}{c_{22}c_{33}-{c_{23}}^2} \quad (2)$$

$$E_{22} = \frac{(c_{11}c_{22}c_{33}+2c_{23}c_{12}c_{13}-c_{11}{c_{33}}^2-c_{22}{c_{13}}^2-c_{33}{c_{12}}^2)}{c_{11}c_{33}-{c_{13}}^2} \quad (3)$$

$$E_{33} = \frac{(c_{11}c_{22}c_{33}+2c_{23}c_{12}c_{13}-c_{11}{c_{33}}^2-c_{22}{c_{33}}^2-c_{33}{c_{12}}^2)}{c_{11}c_{22}-{c_{12}}^2} \quad (4)$$

Table 7. Anisotropic elastic constants matrix with orthorhombic symmetry.

Anisotropic Elastic Constants					
c11					
c21	**c22**		Symmetrical		
c31	**c32**	**c33**			
c41	c42	c43	**c44**		
c51	c52	c53	c54	**c55**	
c61	c62	c63	c64	c65	**c66**

Table 8. Orthorhombic elastic constants and material properties.

Elastic Constant	**$FePO_4$ (Gpa)**	**$LiFePO_4$ (Gpa)**
C11	166.5	133
C22	127.7	203
C33	121.3	172.3
C44	32.5	34.9
C55	43	47.8
C66	45.6	42.4
C12	33	74.3
C13	57.1	54.3
C23	9.2	55.2
Poisson Ratio	0.3	0.23
Shear Modulus (Gpa)	44	45
Bulk Modulus (Gpa)	66	96

3.1.1 Factors for Electrode Failure

Structural failure due to fracturing of active material is a main factor in battery degradation and overall capacitance loss after many cycles of use [24, 25, 29-31].

Each time lithium ions are inserted into the cathode during the discharging process, the anisotropy of the material produces a volumetric change up to 7% occurs which induces misfit strains as the phase transformation from $FePO_4$ to $LiFePO_4$ occurs (Table 9). Stresses induced by the phase transformation strains may create flaws or cracks that will be stress concentration areas when further cycling occurs. A combination of tensile and compressive stresses will induce microscopic crack propagation if critical values are reached. Over time and repeated cycling, fatigue crack propagation will continue for a finite number of cycles until the crack reaches a critical crack length where complete fracture initiates. When this active electrode material is fractured away, the battery will effectively loose capacitance and maximum power output diminishes. Thus, understanding the relationship between stresses and imperfections during lithium ion intercalation will be instrumental.

Table 9. Lattice parameters and misfit strain during lithium insertion for $FePO_4$ and $LiFePO_4$ phases. Letters a, b and c refer to the [001], [010] and [001] planar directions.

	$FePO_4$	**$LiFePO_4$**	**Misfit Strain**
V [Å^3]	288	297	-
a [Å]	9.94	10.39	ε_a = 5.03%
b [Å]	5.93	6.04	ε_b = 3.7%
c [Å]	4.88	4.73	ε_c = -1.9%

During a battery discharging operation, The most prominent stresses arise at the phase boundary interface where tension is applied in the ‘a’ and ‘b’ directions and compression is observed in the ‘c’ direction of $LiFePO_4$ [25, 27, 31, 33] (Fig. 13).

3.2 Simulation Design

Pre-existing cracks in the electrode material are sites for stress concentrations and it is the focus of the current study. ANSYS finite element software (ANSYS, Inc. Canonsburg, Pennsylvania) is utilized to model the phase transformation process at the crack. A scaled up model of a $LiFePO_4$ unit cell measures 200-nm x 120-nm x 90-nm and a crack is considered to run parallel to the bc-plane (along the c-axis) where phase boundaries are present (Fig. 13). Figure 13 shows our finite element model representation, in which L represents the crack length and d represents the particle size. Nine finite element simulations are conducted for cracks of sizes L/d=0.05-0.8, where L is the crack length and d is the length of the particle parallel to the cracking direction.

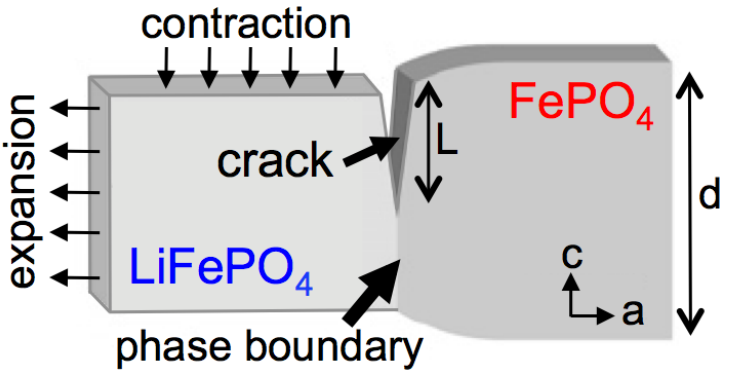

Figure 13. Particles undergo phase changes, in which L represents the crack length and d represents the particle size. Expansion occurs along the a-direction (ε_a = 5.03%), and extraction occurs along the c-direction (ε_c = -1.9%).

Displacements were applied to the $LiFePO_4$ phase according to the misfit strains previously measured and reported in literature (Table 9). This initial flaw is applied from the top face with variable length from 0.05-0.8 L/d and the crack opening is set as 0.5 nm to stay proportional to experimentally observed crack [25]. Assuming displacements along the a- and c-axes are independent of the b-axis and no normal tractions exist on the ac-plane, the plane stress assumption is applied. The model is reduced to a 200-nm x 90-nm 2D plate, viewed on the ac-plane. Although crack propagation is possible in other planes, literature and experimentations report cracks observed in the bc-plane between phases while propagating in the c direction [27]. The olivine crystal structure of $LiFePO_4$ and the Third Pauli's Rule supports this observation: (100) planes are linked through stable, shared corner bonds between FeO_6 octahedra and PO_4 tetrahedra while (010) planes are connected together by weaker, edge-sharing bonds between FeO_6 octahedra [25]. 2D quadrilateral elements of type PLANE 183 are used in our finite element analysis, and the model is densely meshed around the crack tip to a size of $5E^{-10}$ m (Fig. 14). PLANE 183 elements were chosen as the eight

node structure allows for more flexibility and improved accuracy in contrast to four-node, PLANE 182 elements.

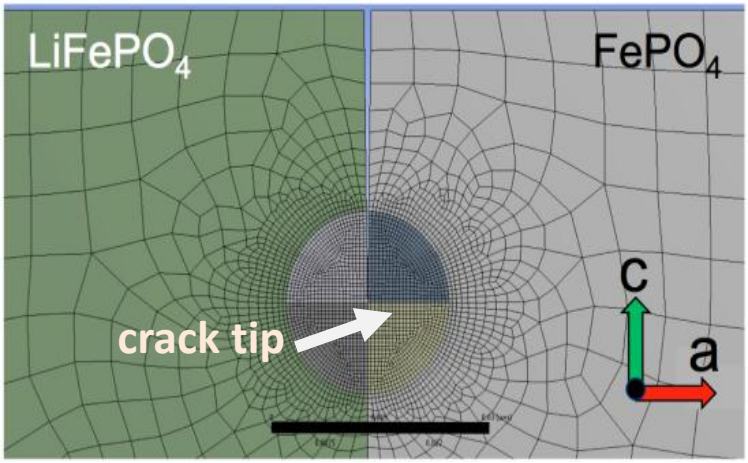

Figure 14. Finite element mesh near the crack tip. Scale bar = 0.03 μm.

First introduced by Irwin, the basis for strain energy release rate (SERR) is to find the change in elastic energy per change in crack size [34]. Energy release rates, also denoted as G, are one of the most important fracture mechanics parameters for isotropic or orthotropic materials and it is part of the basis for linear elastic fracture mechanics. In this study, G values will be utilized with the simple plane stress assumption to elucidate cracking tendency for a given sized crack in a particle under cycling stress. As a crack advances, the surface area of this imperfection increases but the elastic energy in the particle decreases. A crack can no longer propagate if the G valueis less than approximately two times the surface energy of the particle ($G < 2\gamma$) [34].

The rate of discharge will determine resultant stresses within the material which will in turn control the SERR at a crack in the particle. Larger stress in a shorter period of time may induce cracking more readily than for slower discharging rates. This is due to the limited volumetric expansion rate unable to satisfying the rate of lithium diffusivity during fast discharging, similar to rush hour traffic in limited highway space. Therefore, one potential future consideration is to reduce the particle size of $LiFePO_4$ electrode particles to effectively reduce the diffusion path and decrease stress inside the particle [32]. The strain energy release rate is calculated by ANSYS using fracture mechanics based on Irwin's virtual crack closure technique (VCCT) method. The theory behind VCCT is that the energy needed to separate a surface is the same as the energy needed to close the surface back on itself [35]. In other words, the SERR is simply "the work required to change the mid-plane strains and curvatures in the cracked part of the plate at the crack front so that they are equal to the midplane strains and curvatures in the uncracked part of the plate at the crack front" [36]. Using a proper mesh and several commands in ANSYS, the VCCT method calculates relative displacements (u,w,a) and reaction forces (X, Z) (Fig 15) which then are formulated to produce energy release rates found in Table 10.

$$G_I = \frac{-[X_1(\Delta u_1) + X_2(\Delta u_2)]}{2\Delta a} \tag{5}$$

$$G_{II} = \frac{-[Z_1(\Delta w_1) + Z_2(\Delta w_2)]}{2\Delta a} \tag{6}$$

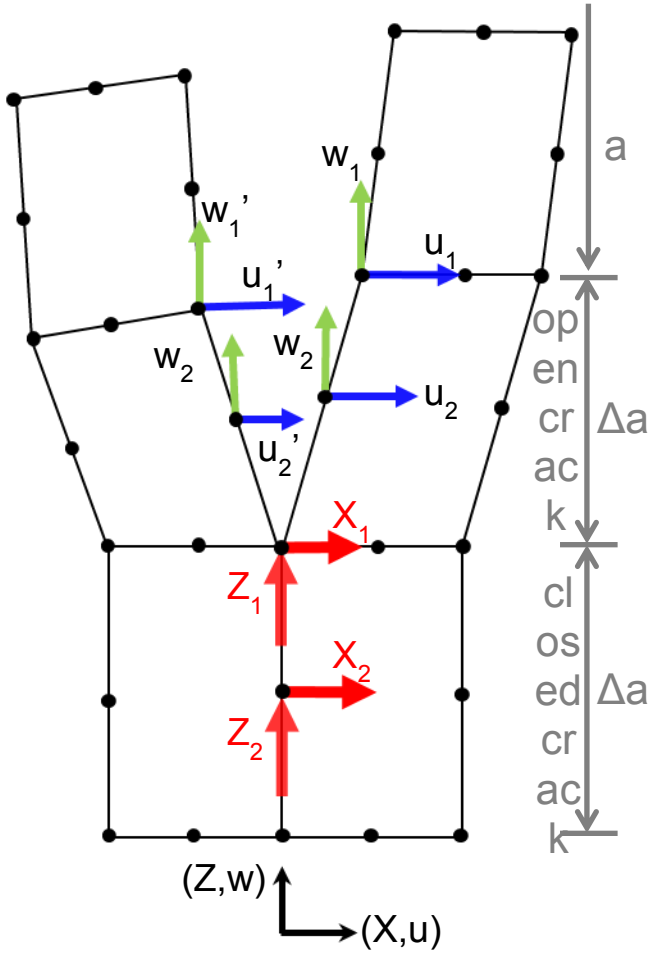

Figure 15. VCCT method for 2D quadrilateral elements. Energy release rates are calculated via the crack size (Δa), reaction forces (Z and X), and relative displacements (u, w, and a).

3.3 Simulation Results

Figure 16 shows the stress fields for an entire particle between phases. Shades of purple and green represent areas of compression and tension, respectively. Shades of white express minimal or zero stress areas. Overall, normal stresses dominate as compared to shear stress throughout the particle.

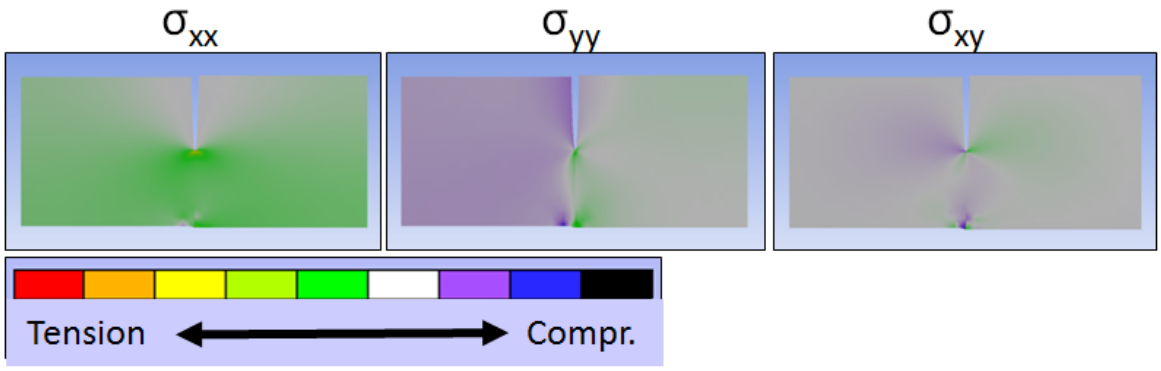

Figure 16. Stress fields for an entire particle between $FePO_4$ phase to the right of the crack and $LiFePO_4$ to the left. L/d=0.5.

Table 10 shows a tabulation of SERR (G) values and stress intensity factors (SIF) data. Mode I (opening) is dominant but Mode II (in plane shear) also contributes. Mode III (out of plane shear) is non-existent in the plane stress model.

Table 10. Strain energy release rates (G, units of N/m) and stress intensity factors (K, units of MPa x $m^{1/2}$) at the crack tip.

L/d	G1	GII	GT	KI	KII
0.05	-0.065	0.003	0.068	0.354	-0.145
0.1	-0.077	-0.002	0.079	0.531	-0.293
0.2	3.088	-0.393	3.481	0.674	-0.187
0.3	4.138	-0.263	4.400	0.779	-0.140
0.4	4.630	-0.220	4.850	0.836	-0.103
0.5	5.075	-0.100	5.176	0.861	-0.069
0.6	5.176	-0.045	5.220	0.902	-0.055
0.7	5.200	-0.011	5.211	0.903	-0.009
0.8	5.294	0.011	5.305	0.926	0.055

GT is the total strain energy release rate, and it is a combination of modes I and II. The cracking mode during the propagation is a resultant of applied stresses, elastic moduli values, and therefore resultant stress intensity factors (K_I and K_{II}) are calculated for each simulation to predict the state of stress around the crack tip. Specific reasoning behind the magnitude of Mode I and Mode II magnitudes directly relates to a combination of misfit strains and anisotropic elastic moduli values. As the a-direction modulus (E_{11}) for $LiFePO_4$ is much smaller than the other orthorhombic directions while the strain in the a-direction is the largest promotes Mode I, splitting or opening, fracturing in this material. Figure 17 reveals that SEER is highly dependent on the crack size as seen with large deviations from small to large cracks.

One critical point starts at around L/d=0.5, where release rates are very high and then begin to level off. If an applied stress is large enough to propagate a crack at L/d=0.5, the

same applied stress will also be large enough to continue propagation for future cycling at larger L/d values (longer cracks than L/d=0.5). Therefore, this is the maximum L/d point that needs to be considered to determine if a crack will extend during lithiation.

Stress intensity factors are also calculated in the study to further delineate differences between Mode 1 and Mode II cracks near the crack tips (Fig. 18).

It is observed that Mode I SIF reaches a relative maximum value of 1.0 when $L/d \geq 0.5$. In contrast, Mode II SIF continues to decrease towards zero (under compression) while cracks become larger. Corresponding stress fields at crack tips for L/d=0.1, 0.4 and 0.7 are shown in Figure 19.

In very short cracks, σ_{yy} contributes the most stress as the particle begins to experience a large magnitude of Mode II (in plane shear) from compression the in the c-direction. But as the cracks grow deeper, σ_{xx} increases showing a transition to Mode I (opening) dominance near the crack tip. τ_{xy} remains small for short cracks but larger compressive stresses develop with crack growth.

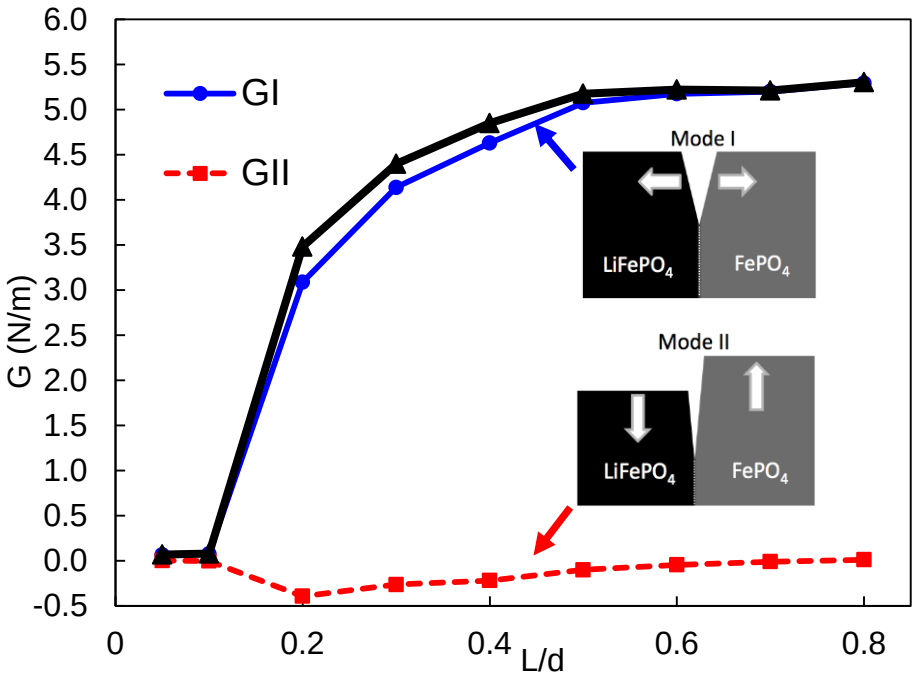

Figure 17. Energy release rates at crack tip for models with nine different L/d ratios. It is observed that Mode I cracks are likely to occur and propagate, especially when L/d $\geq$ 0.5.

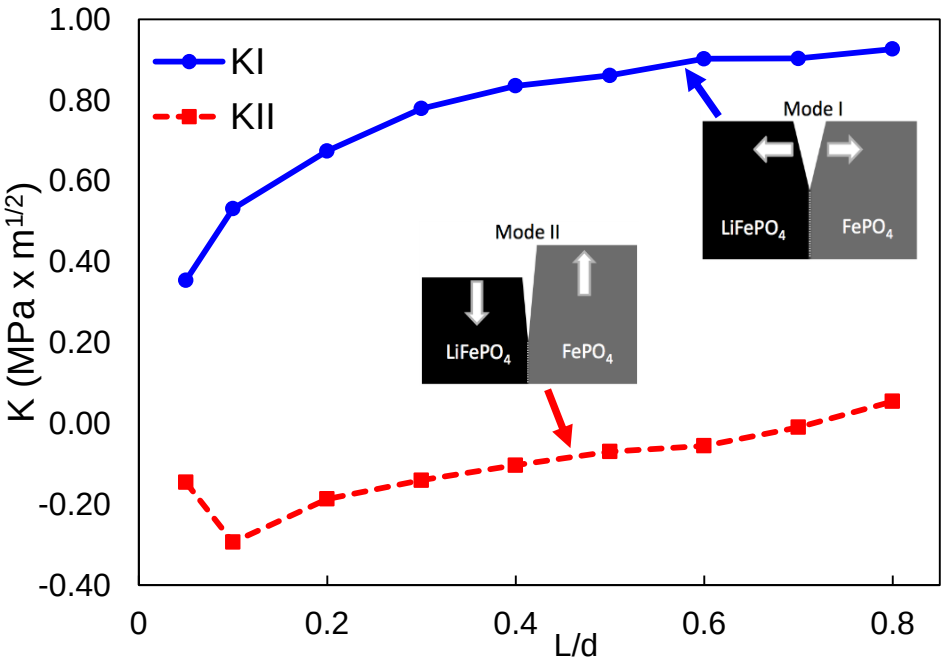

Figure 18. Mode I and Mode II stress intensity factors at crack tips with nine different L/d ratios.

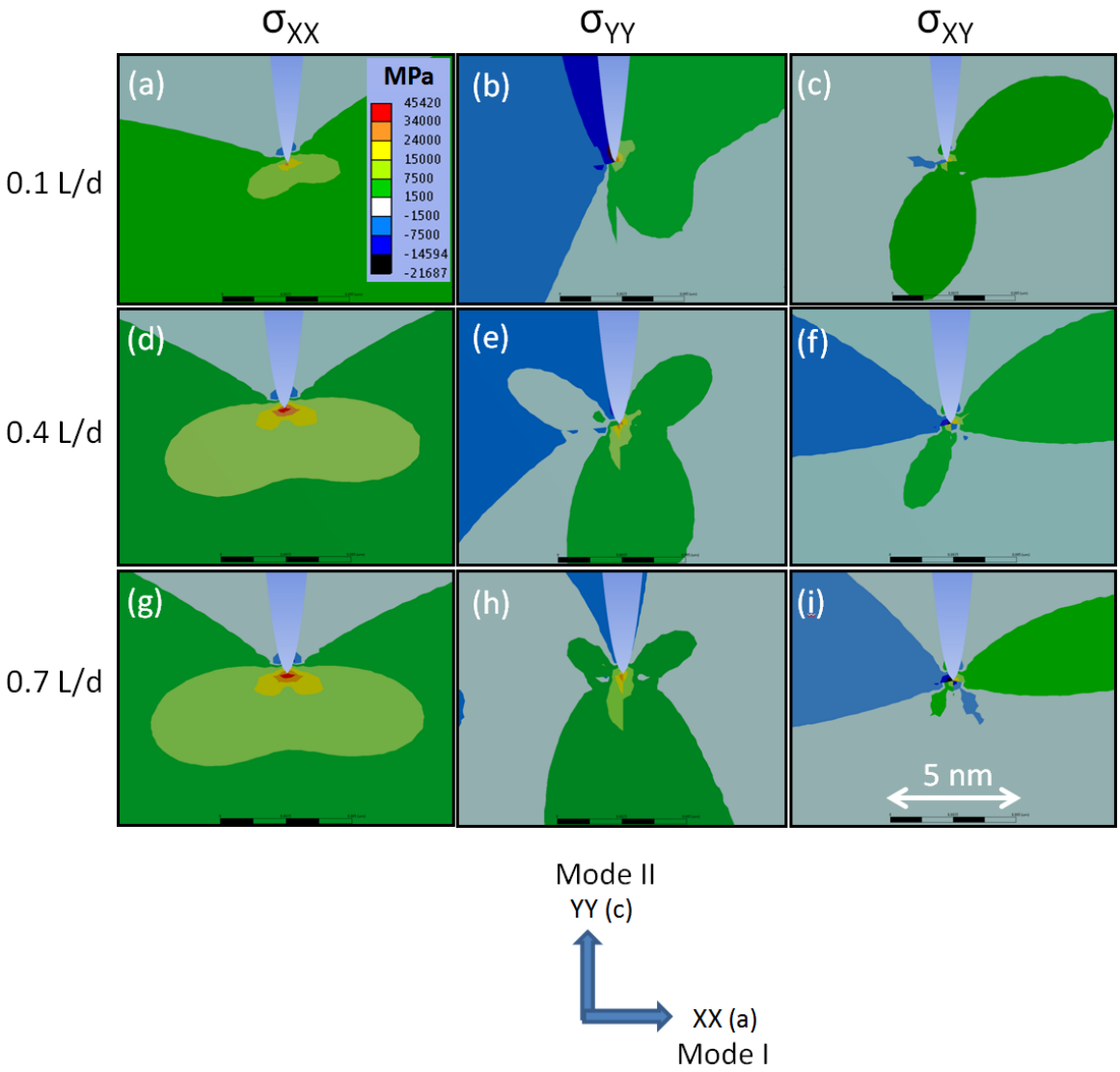

Figure 19. Stress fields for L/d = 0.1, 0.4, and 0.7 show Mode I dominance (σxx dominance) at the crack tip with marginal Mode II (σyy) contribution for smaller cracks and negligible shear stress contributions except for larger sized cracks.

CHAPTER 4 FATIGUE ANALYSIS AND ENERGY APPROACH

It is concluded that cracks propagate to relieve internal stresses while strain energy release rate is the driving force behind these crack propagations. Knowing this, we can apply the following methodology to accomplish our second research objective of establishing theoretical fatigue life estimation for $LiFePO_4$ using ANSYS FEA software simulations.

To predict fatigue crack growth, total strain energy release rates (G_T) and surfaces energies ($\boldsymbol{\Upsilon}$) are compared and allow for propagation when $G>2\boldsymbol{\Upsilon}$. A first-principles analysis by Wang et al reports a $\boldsymbol{\Upsilon}$ value of 0.66 N/m for $LiFePO_4$ on the (100) plane which represents the usual crack face orientation [37]. This value is consistent experimental data from other types of covalent/ionic ceramic materials that show surface energy values of 0.5-1.5 N/m [38]. Once G_T increases above 1.32 N/m, crack propagation is eminent and a crack will grow until the surface energy from newly formed crack faces returns the particle back into equilibrium with the strain energy release rate. Depending on initial crack surface area and the obtained G_T value during cycling, a difference in energy is calculated,

$$\Delta E = G-2\boldsymbol{\Upsilon} \tag{7}$$

If ΔE is positive, a crack will grow until the crack surface energy is greater than or equal to G_T. The following describes the formulation and variables for determining crack propagation length per cycle for a particle with a crack on the b-c face with a 'b' dimension of 120nm.

4.1 Sample Calculation

The formulation for a crack length of L/d=0.3 is provided where G_T=4.40 J/m^2 from ANSYS simulation and $\boldsymbol{\Upsilon}$=0.66 J/m^2 from literature. This analysis sets the value of one unit length of propagation equal to 0.01nm.

E_s : particle surface energy per 0.01nm of crack extension

E_R : energy per 0.01nm due to strain energy release rate

A_N : the new surface area per 0.01nm crack extension

α : equal to E_R/E_S, gives the number of unit lengths needed for equilibrium

da : crack extension length per one cycle

$$\Delta E = 4.40\frac{J}{m^2} - 1.32\frac{J}{m^2} = 3.08\frac{J}{m^2}$$

$$A_N = b \times l \tag{8}$$

$$A_N = 120nm \times .01nm = 1.2E^{-18}\, m^2$$

$$E_R = b \times l \times \Delta E \times 2 \tag{9}$$

$$E_R = 120nm \times .01nm \times 4.755E^{-18}\frac{J}{nm^2} \times 2 = 7.393E^{-18}\ \text{J}$$

$$E_S = A_N \times \Upsilon \times number\ of\ cracks\ (2) \tag{10}$$

$$E_S = 1.2E^{-18}J \times 0.66\ \frac{J}{m^2} \times 2 = 1.584E^{-18}\ J$$

$$\alpha = \frac{E_R}{E_S} \tag{11}$$

$$\alpha = \frac{7.393E^{-18}\,J}{1.584E^{-18}\,J} = 4.77584$$

$$da = \alpha \times .01nm = .047758\,nm = 4.7758E^{-11}\,m$$

The calculation shows α = 4.77584 unit lengths, thus 0.047758 nm of crack advancement are required to reach equilibrium during this single lithium insertion cycle.

An iterative MATLAB program is then utilized to recalculate the required energy and crack length advancement until insipient fracture or until the crack is assumed large enough to be detrimental to further lithium cycling (Fig. 20) near L/d=0.8.

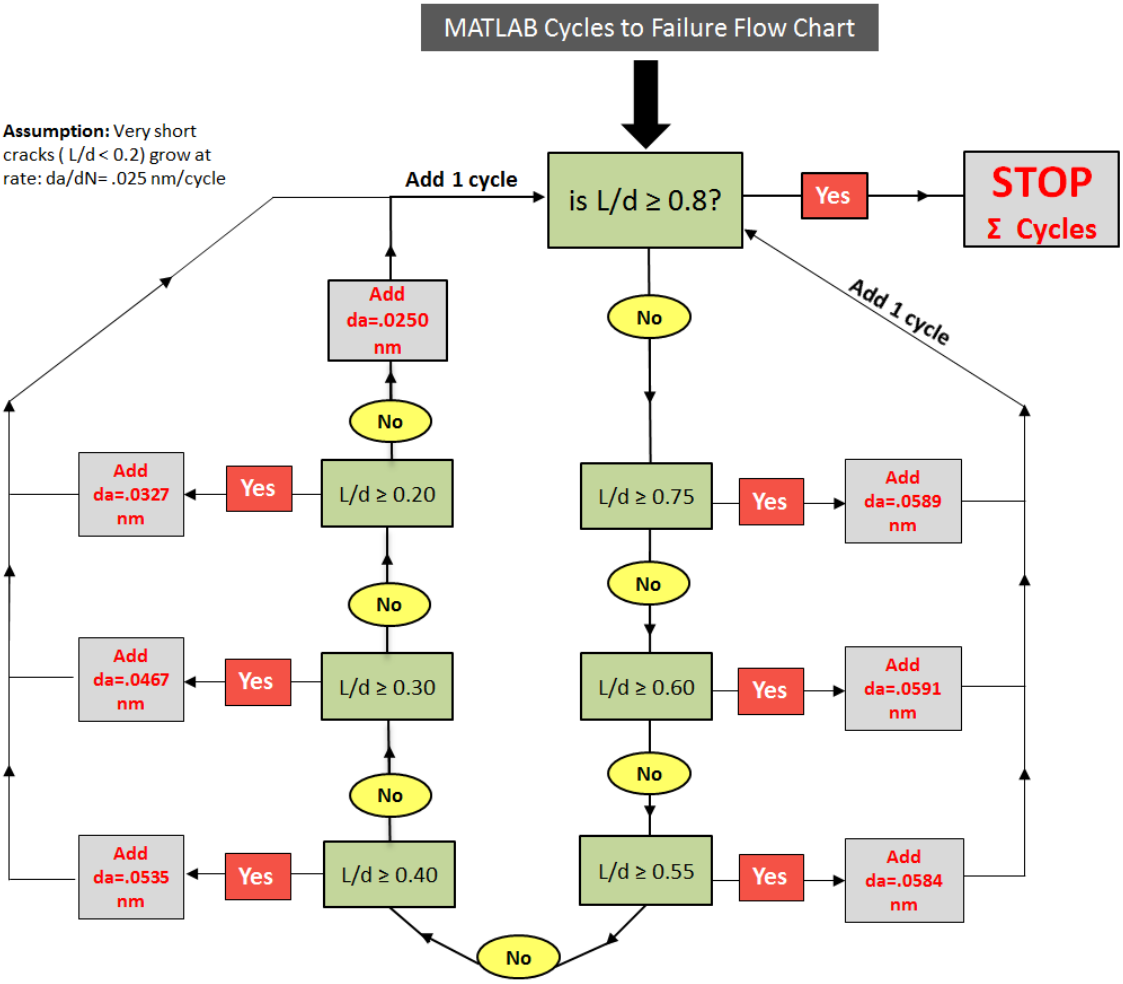

Figure 20. Flow chart depicting MATLAB algorithm for cycles to failure calculation.

4.2 Paris Plot and Fatigue Life Estimates

The following example of a fatigue plot for A533B-1 steel shows three regions: region I denotes the threshold region where only minute crack growth occurs; region II is the Paris Law region in which primary fatigue crack growth occurs (shaded green), and region III is a critical threshold zone where the stress intensity factor may exceed the fracture toughness of the given material causing incipient fracture to occur. The fracture toughness, Kic, and fracture threshold region, Kth, is unknown for $LiFePO_4$ thus this research will only focus of creating a simulation method to obtain region II data for primary fatigue crack growth.

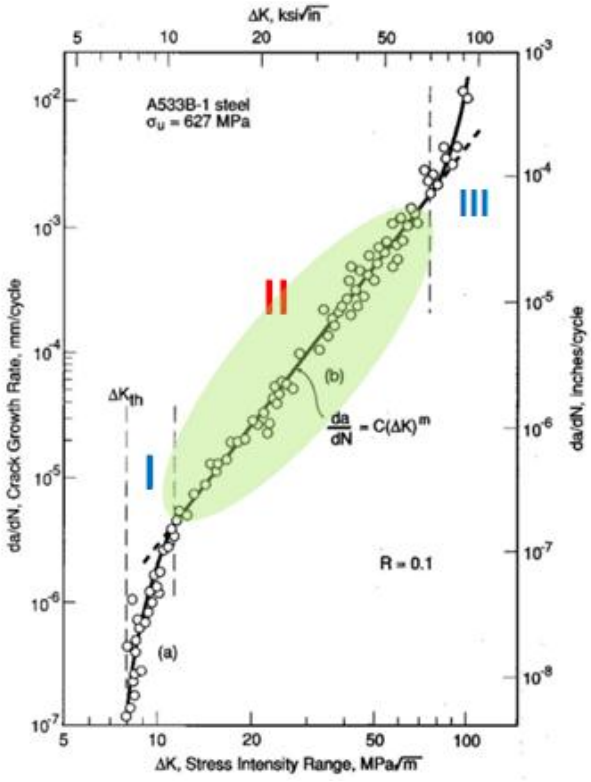

Figure 21. Example of a Fatigue Life Cycle Plot for A533B-1 steel. The green shaded region is Paris' power law and shows the portion of primary fatigue crack growth.

A simulated estimate for the fatigue life of $LiFePO_4$ is created by generating da crack progressions using SERR and surface energy values as described in section 4.1. These values are plotted with the accompanying ΔK value which is simply the maximum recorded stress minus the minimum. As the ANSYS simulation only cycles to a maximum and back to zero, the ΔK is essentially the dominating Mode I stress intensity factor measured in ANSYS. Figure 22 shows the resulting fatigue life plot for $LiFePO_4$ which is described by the Paris Law relationship. The cumulative number of cycles until fracture, depending on initial crack size, is then recorded and plotted against the actual L/d dependent crack lengths (Fig. 23a and 23b).

$$\text{Paris Law: } \frac{da}{dN} = C\Delta K^m \tag{12}$$

The crack growth rate term on the left side represents the infinitesimal crack length growth per load cycle where '*a'* is the crack length and '*N'* is the number of load cycles. On the right side of the equation, *C* and *m* represent material constants of $LiFePO_4$, and ΔK is the difference in observed difference in maximum and minimum stress intensity factor during the cycling simulation.

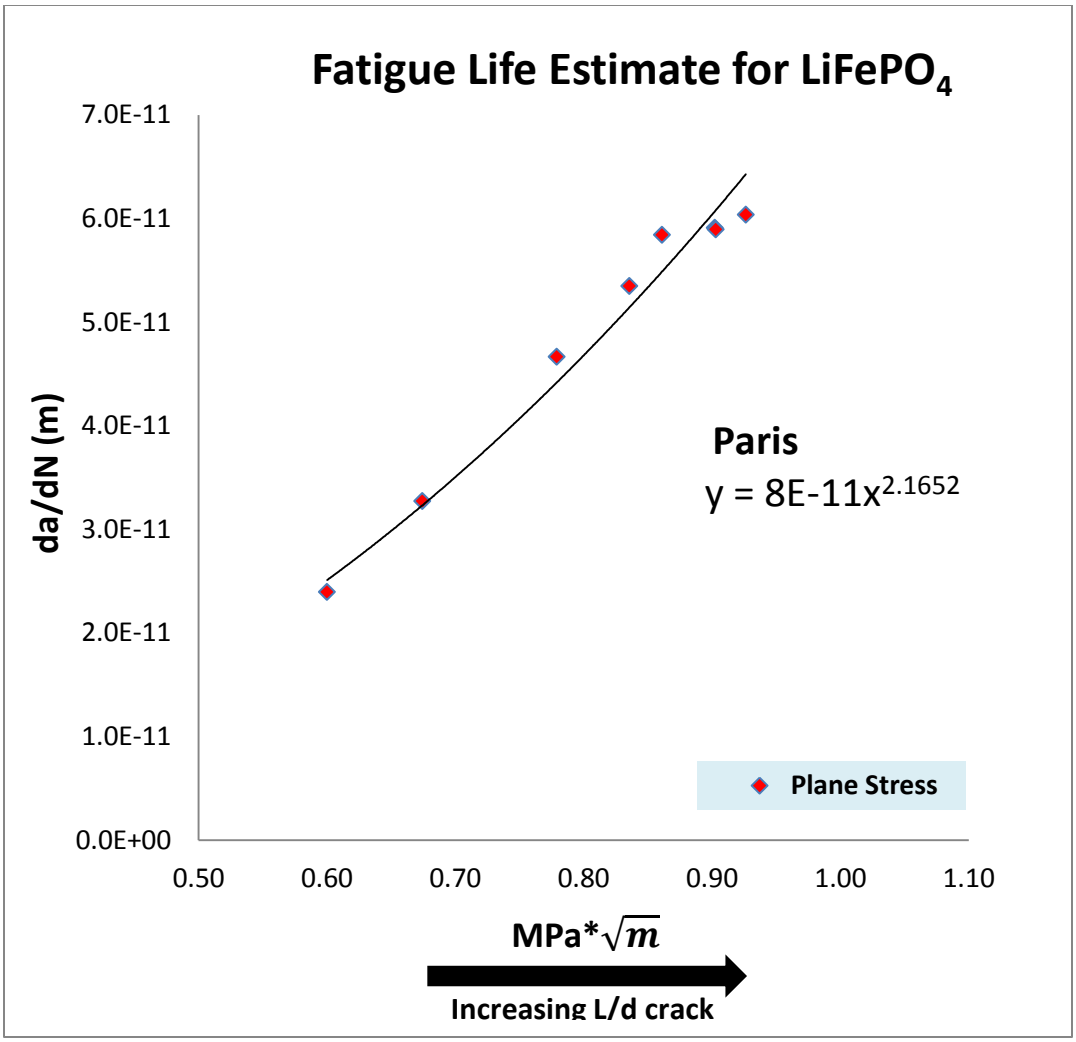

Figure 22. SERR and SIF data is obtained from ANSYS FEA software and is applied to the energy fatigue approach in order to develop the fatigue life plot. The Paris Law is fit to the data and reveals the following best fit constants: C=8x10-11 and m=2.1652.

a.

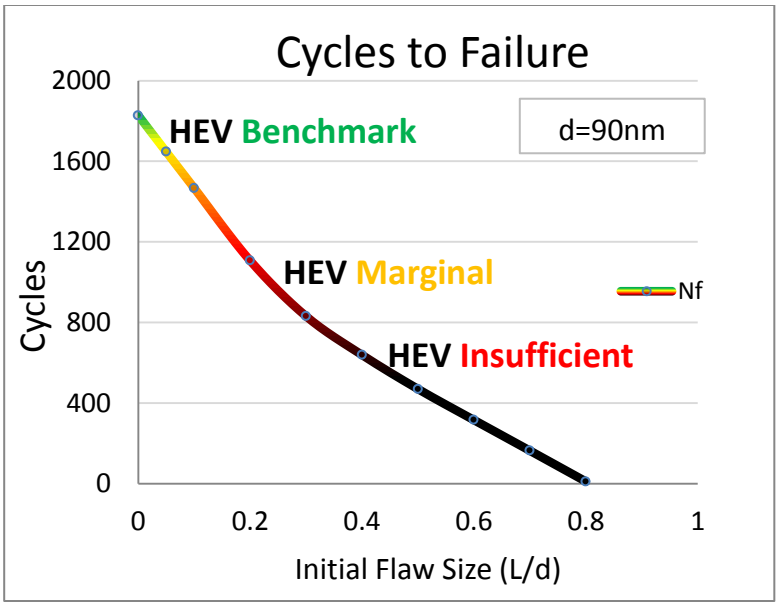

b.

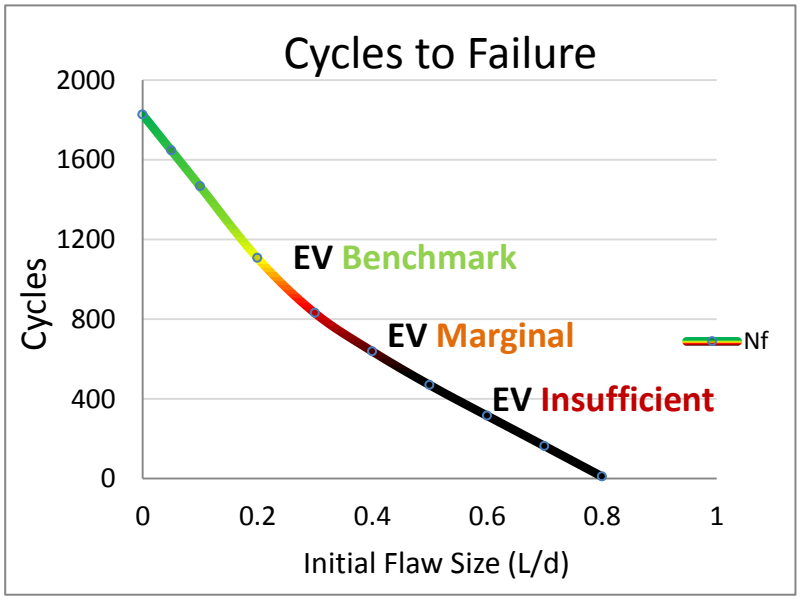

Figure 23a & 23b. A maximum value of approximately 1800 cycles is attained with 0.1 nm size initial flaw for the 90nm $LiFePO_4$ particle. Cycles decrease steadily as initial flaw size increases. HEV and EV cycle life performance is represented on graphs a and b, respectively. The green to yellow to red color transition represents good to marginal values, yellow to orange represents marginal, and red to black represents unsuitable cycle life according to the USCAR.

The USCAR (United States Council for Automotive Research LLC) reports benchmark objectives of 10 years (EV) and 15 years (PHEV) for all future batteries [39]. One popular cathode material currently in production for the Chevy Volt and Nissan leaf is $LiMn_2O_4$. With this type of cathode chemistry, the U.S. Department of Energy research shows that a Chevy Volt PHEV undergoes 17 partial charging events per month and a Nissan Leaf EV can travel about 70 miles per full charge [40]. Assuming this data equates to about 2 full charges per week per vehicle, calculations indicate the need for 1050 (EV) and 1550 (PHEV) cycles until dead on discharge to meet the 10 and 15 year requirement, respectively. EV vehicles have a lower cycle life requirement as the battery is used for primary power unlike HEV that uses the battery as complimentary power to a combustion engine [39].

The feasibility of using $LiFePO_4$ cathode batteries with these stipulations can be assessed with Figure 23 by taking into account the Weibull distribution of damaged particles. A Weibull distribution is a continuous probability distribution that, in the case of a cathode material, can describes the percentage of severely damaged, marginally damaged and flawless particles in the bulk material. According to a study on $LiCoO_2$, a comparable cathode material, severely strained particles exhibiting micro cracks and dislocation defects account for 20% of the total examined, 50% show small signs of damage and 30% remain unaffected during cycling [41]. This allows the assumption that the 50% portion of marginally damaged particles will drive the overall performance and the particle should perform to at least 80% of its theoretical capacity and life cycle expectations if the severely damaged particles are taken into account. Thus, if 50% of particles initially have 0.20 L/d sized defects or smaller, $LiFePO_4$ can achieve the EV requirement of 1050 cycles.

Additionally, initial sized defects of size 0.075 L/d or smaller allow the material to achieve the 1550 cycles requirement for PHEV.

In order to provide some measure of validation for this method, a simplified simulation for stainless steel was compared to experimental results from literature. The following properties, as listed in the default ANSYS material library for stainless steel, and loading model were utilized in the simulation for a 2D plate under the plane stress condition (Fig. 24).

Young's Modulus = 193 GPa

Shear Modulus = 74 GPa

Bulk Modulus = 169 Gpa

Poisson Ratio = .31

Ult. Tens. Strength = 586 Mpa

Surface Energy = .85 N/m

Variable force: 0.25 N – 2.0 N (to produce a ΔK range of 5-65 MPa$\sqrt{m}$)

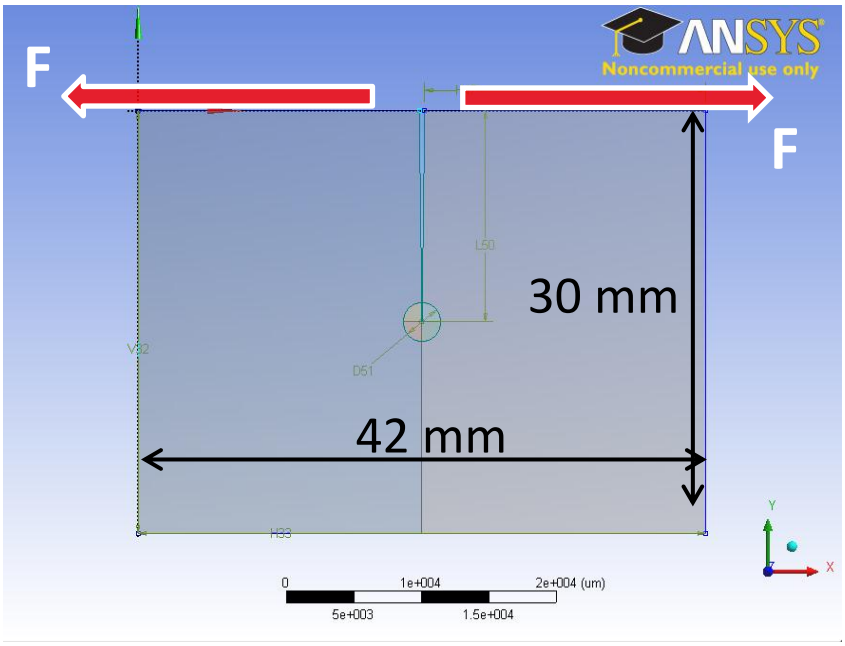

Figure 24. Steel simulation setup and loading.

As obtained from literature, a fatigue life model for a type 316L stainless steel following the compact tension specimen setup from the ASTM e647 Standard (Fig. 25) was compared to our simulation [42]. The inputs for both models utilized a young's modulus of 193 GPa, but several differences must be noted between geometry sizing, location of loading, loading ratio and slightly differing strength properties. The ASTM model from literature is a much larger specimen measuring 120.6mm x 115.8mm x 24.1mm ($l\ x\ w\ x\ h$) while the ANSYS simulation measures 30mm x 42 mm with a thickness approaching zero mm as the plane stress condition is applied. Loading for the ASTM model is applied by inserting pins inserted into previously drilled holes on either side of the machined opening, and then applying equal and opposite forces to produce loading ratios of .1 and .8 (minimum peak stress divided by maximum peak stress). The ANSYS simulation simply pulls the top edges

apart with a loading ratio of zero (minimum stress equal to zero), but both procedures produce Mode I fracture. Although the simulation is a greatly simplified model as compared to the ASTM e647 standard, once comparable ΔK values are obtained by manipulating the applied forces, energy release rates can be extracted from the simulation and used to create a basic model for steel fatigue life comparison.

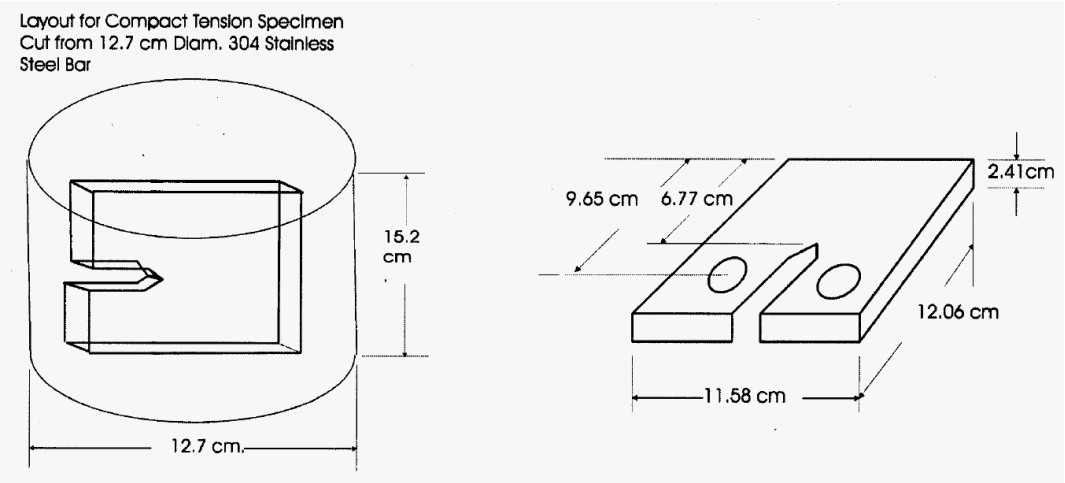

Figure 25. Compact tension specimen from ASTM e649 Standard for fatigue life testing [42].

Results show a similar trend for both models (Figs. 26 and 27), but the 'C' Paris law constant differs by a factor of 1 while the 'm' Paris constant is fairly close at 2.0082 for the steel simulation and 1.77 for experimental data. These differences lead to the ANSYS simulation predicting crack growth per cycle at differing ΔK ranges at 1-2 orders of magnitude smaller, which would contribute to a much larger cycle life prediction. A better agreement may be obtained if the simplified simulation was more robust and followed the

ASTM e647 Standard to show a true comparison. But as this is only a first attempt into estimating the fatigue life plot for $LiFePO_4$, as never before attempted in known literature simulations or experimentation, only a general trend for result agreement was estimated.

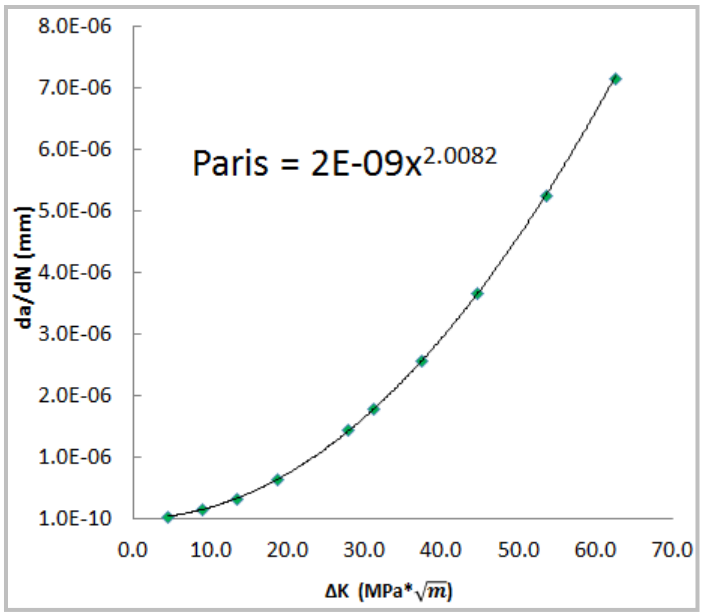

Figure 26. ANSYS stainless steel simulation fatigue Paris plot.

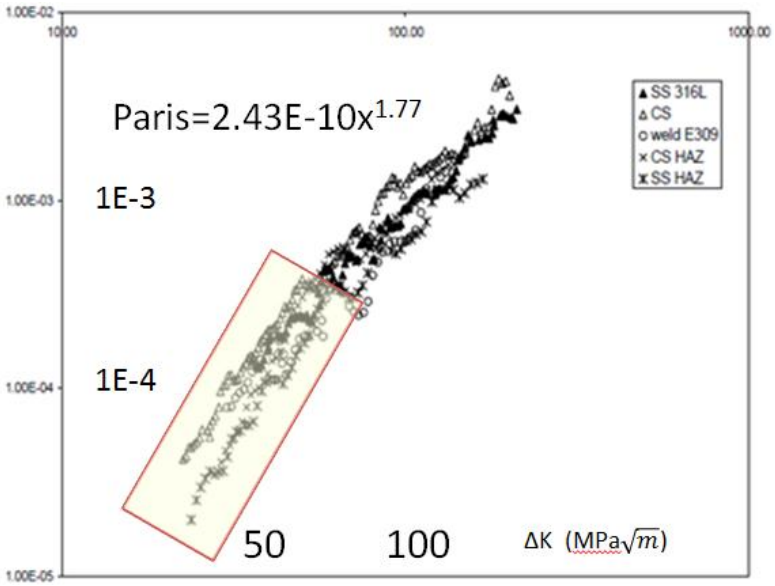

Figure 27. Experimental fatigue Paris plot for 316L stainless steel. Only the shaded box region is compared to the ANSYS driven simulated fatigue plot [42].

The general applicability of this method for these differing material types, ceramic like $LiFePO_4$ and stainless steel metal is not known, but results for $LiFePO_4$ shows very reasonable results when comparing cycles to failure to listed manufacturer specs (Fig. 23). Improving the accuracy of energy release rate contribution towards crack rate extension in sub critical G levels needs to be applied to improve upon errors in under calculating crack extension results. Fracture toughness testing of this material would also be beneficial to more accurately describe the three regions of the fatigue life Paris plot (threshold region where minimal crack extension occurs, the Paris region of primary fatigue crack growth, and failure region where insipient fracture occurs).

It is still the hope of the authors that full nano-scale experimentation be performed to more accurately assess fatigue crack growth rates involving different sized particle, cracks sizes and charging rates.

4.3 Size Effect Comparison to 500nm and 100 nm Particles

Two additional simulations are added for a size effect comparison between strain energy release rate plots and calculated cycle life. The initial simulation already presented incorporated a scaled up unit cell particle of dimensions 200nm x 90nm which is analogous to a 20 x 20 unit cell configuration. A larger particle measures 500nm x 225nm and is analogous to about 50 x 50 unit cells while a smaller simulation has dimensions of 100nm x 45nm and is about equal to a 10 x 10 unit cell configuration. Note that the continuum

assumption still applies to all models as continuum doesn't break down unless particle sizes are less than about 20nm.

The similar procedure was followed for all simulations with only loading conditions being altered to give correct particle deformation and stress distribution based on particle-size dependent strain misfit. Also, a smaller number of simulations were developed (only L/d= .05, .1, .2, .3, .4 and .6) as the basic trend for larger cracks was already known to stabilize around .5 or .6 L/d.

Paris fatigue plots and plots of cycle life vs. initial flaw size were also created for comparison to the previous simulation. Results show that as particle size decreases, lower energy release rates are induced, thus a smaller driving force for crack propagation is present which leads to an overall increase in cycle life. The trend of smaller cracks sizes showing greater sensitivity to energy release rates holds for all sized particles and G rates are seen to level off near 0.5 or 0.6 L/d regardless of particle size as well (Fig. 17, 28, 29).

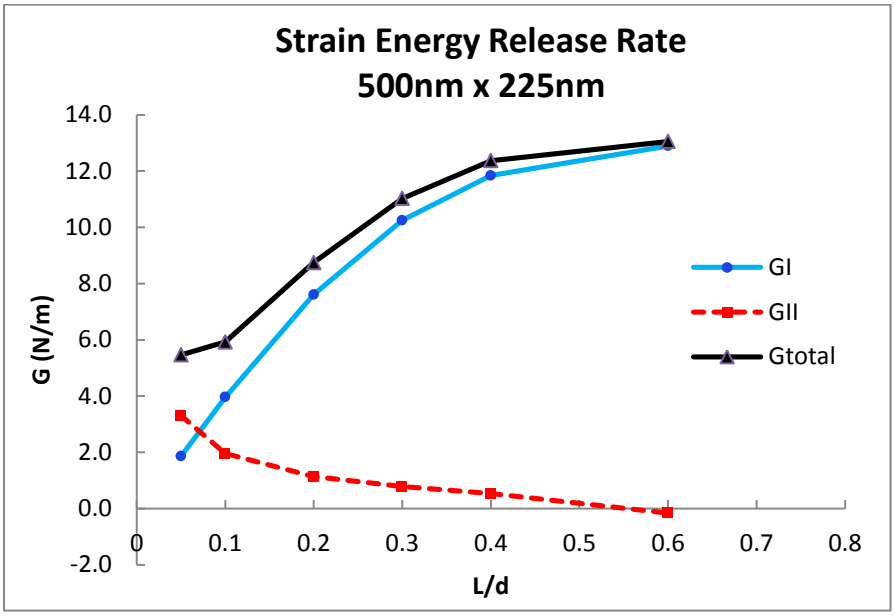

Figure 28. G values for larger particle, 500nm x 225nm.

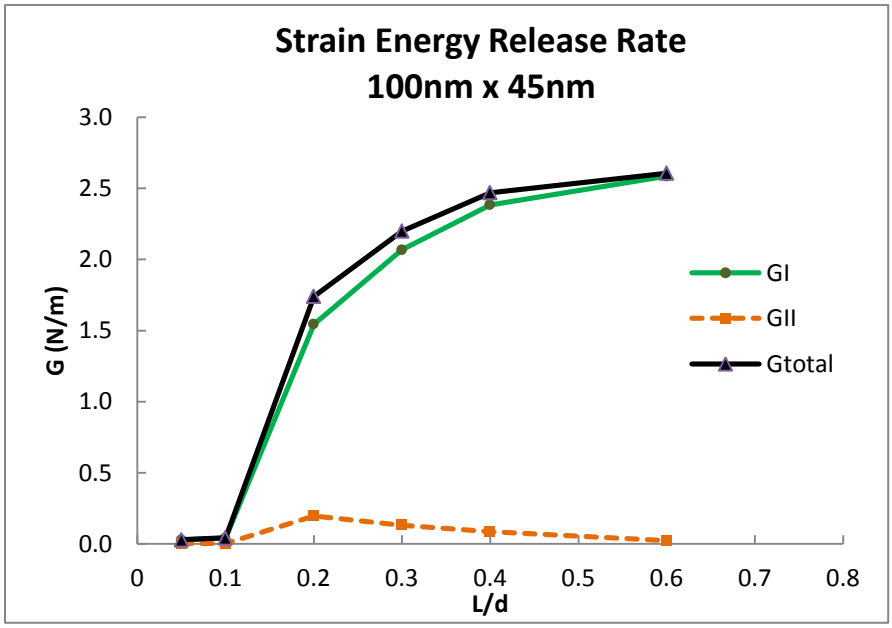

Figure 29. G values for smaller particle, 100nm x 45nm.

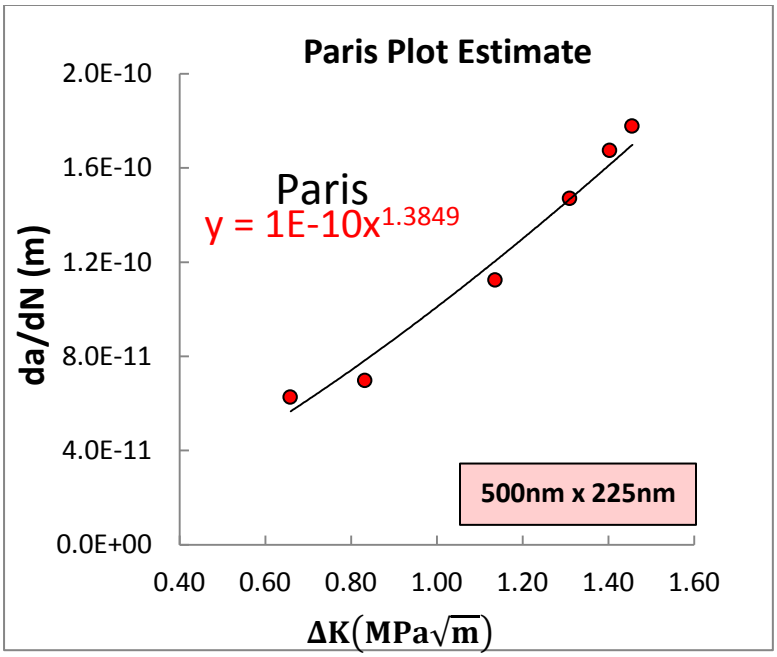

Figure 30. Fatigue Paris Plot for 500nm sized $LiFePO_4$ particle.

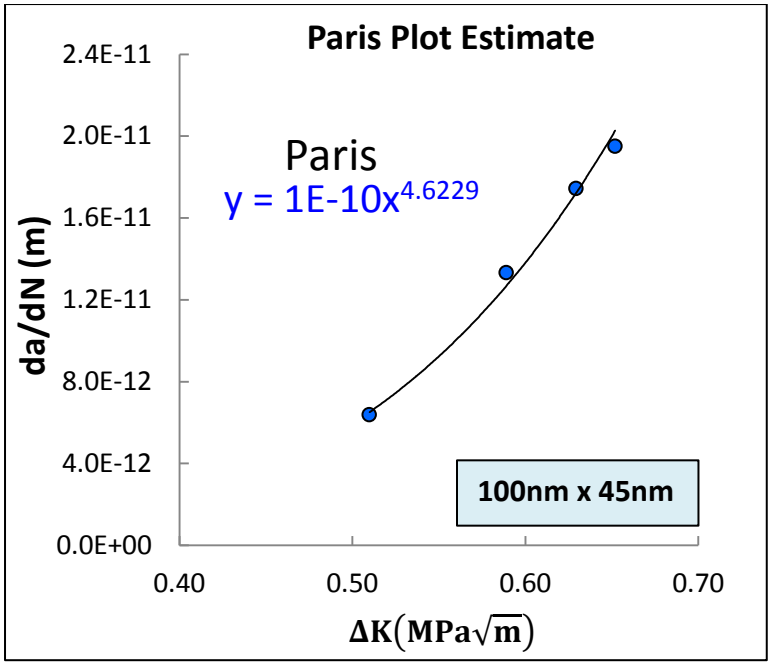

Figure 31. Fatigue Paris Plot for 100nm sized $LiFePO_4$ particle

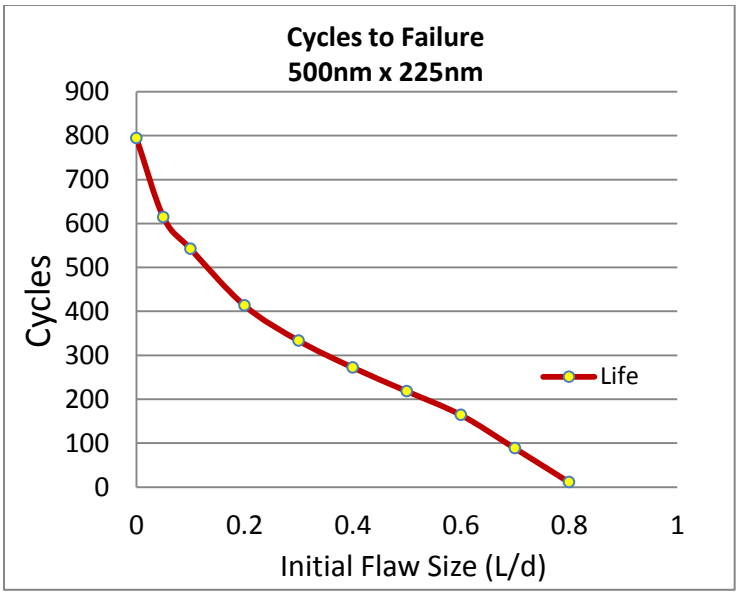

Figure 32. 500 nm cycle life plot versus initial flaw size.

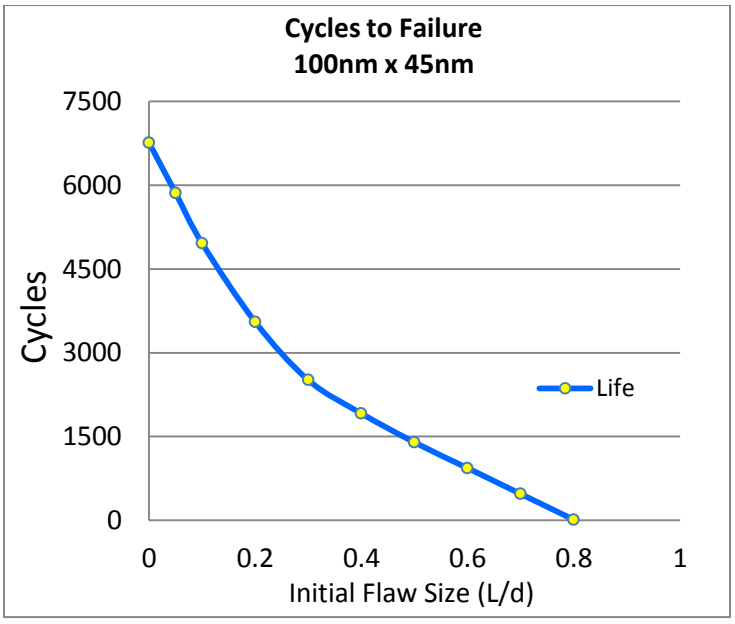

Figure 33. 100nm cycle life plot versus initial flaw size.

Figures 30 and 31 show Paris plots due to energy release rates and stress intensity factors. The smaller and larger particles show a Paris m constants of 4.6229 and 1.3824, respectively; while both give a C constant of $1x10^{-10}$. These constants are calculated empirically in practice but are currently unknown and thus are estimated in this paper based on the energy fatigue approached outlined earlier. It's known that C and m are dependent basic material properties but may also be influenced by the size of a test specimen.

When comparing Figures 32 and 33, small particles are capable of significantly longer cycle lives. Comparing cycles to failure shows 100nm particles could last about 4 times as long as 200nm particles and 8 times that of the 500nm type. Note that all contributors that may alter cycle life such as diffusion interactions or external influences such as temperature influences are not considered separately, but the particle size to cycle life relationship is still captured by modeling with lattice misfit boundary conditions at room temperature. It is also assumed that the cell is charged and discharged completely for each cycle.

In theory, reducing particle size is thought to effectively reduce the diffusion path and decrease internal stress within the particle and increase cycle life [32]. But the limit to which an advantage is gained by decreasing particle size is currently unknown and requires further simulation and experimentation.

4.4 $LiCoO_2$

The same analysis that was applied to $LiFePO_4$ in this study can be altered to allow for adaption to other electrode materials such as $LiCoO_2$. Figure 34 shows results when this procedure is run for $LiCoO_2$ after certain parameters are altered for changes in strain misfit, material properties and dimensions based on the crystal structure lattice constants. Additional parameters may need to be added based on the material being studied. For example, the accuracy of Figure 34 could be improved if thermal stress contributions were added as $LiCoO_2$ is known to produce a significant exothermic reaction which may also alter strength properties.

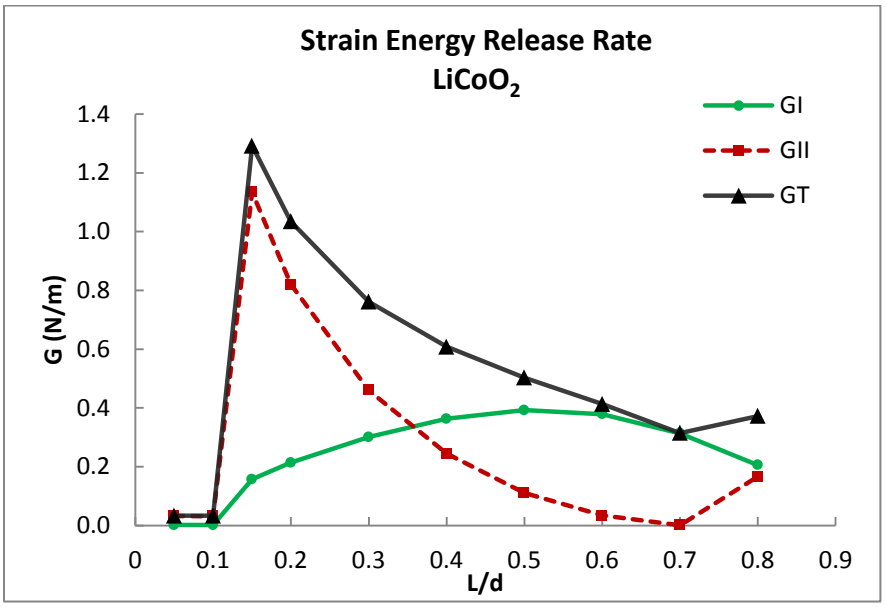

Figure 34. $LiCoO_2$ energy release rate per initial crack size.

CHAPTER 5 SUMMARY AND CONCLUSIONS

In summary, the foundation for a fatigue analysis of lithium-ion cathode materials is provided. Material properties are obtained from literature and ANSYS FEA software is utilized to model flawed $LiFePO_4$ particles and generate strain energy release rates (G) and stress intensity factor (K) data. ANSYS simulations can then be compared to two times the crack-face surface energy of the particle to determine if a crack will propagate. Results show that there is a maximum region for G near the point of L/d=0.5 that remains stable up until complete fracture. Thus, if this point of maximum energy release rate is not great enough to cause cracking, propagation may be subdued if cycling is continued at the same rate. If this value is great enough to cause propagation at a set discharge rate, the induced stress will assure fatigue crack propagation until fracture. Cracking modes were also taken into consideration showing strong Mode II fracture type for very short cracks, which gives way to Mode I dominance in intermediate and very long cracks (Fig. 19). A fatigue life plot is presented after comparing strain energy release rates and surface energy of the initially fractured surface. Cycle life results show a theoretical life limit near 1800 cycles which is near reported values in literature and manufacturer websites [43, 44].

5.1 Future Work

This is a first approach towards improving battery structural design by providing a better understanding of micro-mechanics and a base for future fatigue analyses which may

incorporate a variety of electrode materials and additional fatigue life parameters. Although the simulation does not show the contributing effects of charging rate (C-rate), it is known that increasing the C-rate will effectively induce a greater stress on the electrode material which will in turn increase crack propagation and fracture. This is due to the limiting rate of lithium diffusion based on the material's crystal structure and confined 1-D diffusion channels.

Two other parameters in addition to C-rate testing that could use further analysis include evaluating different nano-layer coatings to increase electronic conductivity and fracture toughness along with reducing particle size to effectively reduce the diffusion path, decrease dislocation density, and decrease internal stress within the particle [32]. Our results show that as you decrease particle size, a smaller driving force for crack propagation is predicted as strain energy release rates are smaller. But experimentation and cost analysis estimates are needed to truly determine a critical particle size where the benefits of decreasing size outweigh the higher manufacturing costs and any detrimental effects that may be introduced when the continuum mechanics break down.

This research is intended to help elucidate relationships between cathode micro-mechanics and battery cycle life to one day help guide in the design of a higher performance, longer lasting battery for the future.

REFERENCES

[1] Chung, S. Y., Bloking, J. T., and Chiang, Y. M., 2002, "Electronically Conductive Phospho-Olivines as Lithium Storage Electrodes," Nature Materials, 1(2) pp. 123-128.

[2] American Physical Society 2012, "Lithium Ion Batteries".

[3] Cheon, S. E., Kwon, C. W., and Kim, D. B., 2000, "Effect of Binary Conductive Agents in $LiCoO_2$ Cathode on Performances of Lithium Ion Polymer Battery," Nature Materials, 1(2) pp. 123-128.

[4] Shaju, K. M., and Bruce, P. G., 2008, "Stoichiometric Nano-LiMn2O4 Spinel Electrode Exhibiting High Power and Stable Cycling." Chem. Material, 20(17) pp. 55-62.

[5] Donovan, J., 2011, "Storing Volts," UBM/Avnet Drive for Innovation, 2011(10/10) p. 1.

[6] National Highway Traffic Safety Administration, NHTSA, 2011, "2016 Policy Minimum Requirements".

[7] Howell, D., Duong, T., Deppe, J., 2008, "U.S. Department of Energy's Material Research for Advanced Lithium Ion Batteries: DOE Vehicle Tech Program," Material Matters, 3(4) pp. 100.

[8] U.S. Energy Information Administration, 2011, "2010-2011 Statistics," EIA.

[9] Energy Information Administration, U.S., 2009, "Emissions of Greenhouse Gases in the United States", U.S. Department of Energy DOE/EIA 0573(2008), Office of Energy.

[10] U.S. Energy Information Administration, EIA, 2011, "Annual Energy Review".

[11] U.S. Energy Information Administration, EIA, 2010, "Annual Energy Review".

[12] Chen, and Beharouak, 2009, "Argonne's Lithium-Ion Battery Research Produces New Materials and Technology Transfer Successes," Transportation Forum, 9(2) pp. July 20.

[13] Huang et all, 2011, "Ultrafast Electrochemical Lithiation of Individual Si Nanowire," Nano Letters, 11(6) pp. 2251-2258.

[14] Daiwon, C., Wang, W., Viswanathan, V. V., 2010, "Low Cost, Long Cycle Life, Li-Ion Batteries for Stationary Applications," Pacific Northwest National Lab, DOE.

[15] Liwen, J.e.a., 2011, "Multilayer nanoassembly of Sn-nanopillar arrays sandwiched between graphene layers for high-capacity lithium storage," Lawrence-Berkely National Lab.

[16] Balke et all, 2010, "Nanoscale mapping of ion diffusion in a lithium-ion battery cathode," Oak Ridge National Lab.

[17] Reid, M., Concha, 2007, "Lithium Iron Phosphate Cell Performance Evaluations for Lunar Extravehicular Activities," NASA Glenn Research Center.

[18] Newton, K., 2011, "Marshall Center's Bassler Leads NASA Robotic Lander Work," 2011(August).

[19] Padhi, A. K., Nanjundaswamy, K. S., and Goodenough, J. B., 1997, "Phospho-Olivines as Positive-Electrode Materials for Rechargeable Lithium Batteries," Journal of the Electrochemical Society, 144(4) pp. 1188-1194.

[20] Xia, Y., Fujieda, T., and Tatsumi, K., 2001, "Thermal and Electrochemical Stability of Cathode Materials in Solid Polymer Electrolyte," Journal of Power Sources, 92(1-2) pp. 234-243.

[21] Gao, J., Jianjun, L., Xiangming, H., 2001, "Synthesis and Electrochemical Characteristics of $LiFePO_4$/C Cathode Materials from Different Precursors," Int. J. Electrochem Sci., 6pp. 2818-2825.

[22] Bai, Y., Qiu, P., Wen, Z., 2010, "Improvement of Electrochemical Performances of LiFePO4 Cathode Materials by Coating of Polythiophene," Journal of Alloys and Compounds, 508(1) pp. 1-4.

[23] Delacourt, C., Poizot, P., Tarascon, J. M., 2005, "The Existence of a Temperature-Driven Solid Solution in Li_xFePO_4 for c<x<1”," Nature Materials, 4pp. 254-260.

[24] Zhao, K., Pharr, M., Vlassak, J. J., 2010, "Fracture of Electrodes in Lithium-Ion Batteries Caused by Fast Charging," Journal of Applied Physics, 108(7) pp. 073517.

[25] Gabrisch et al, 2008, "TEM Study of Fracturing in Spherical and Plate-Like LiFePO4 Particles," Electrochemical and Solid-State Letters, 1193 pp. A25-A29.

[26] Chen, G. Y., Song, X. Y., and Richardson, T. J., 2006, "Electron Microscopy Study of the LiFePO4 to FePO4 Phase Transition," Electrochemical and Solid State Letters, 9(6) pp. A295-A298.

[27] Meethong, N., Huang, H. S., Speakman, S. A., 2007, "Strain Accommodation during Phase Transformations in Olivine-Based Cathodes as a Materials Selection Criterion for High-Power Rechargeable Batteries," Advanced Functional Materials, 17(7) pp. 1115-1123.

[28] Meethong, N., Huang, H. S., Carter, C. W., 2007, "Size-Dependent Lithium Miscibility Gap in Nanoscale Li1-xFePO4," Electrochemical and Solid State Letters, 10(5) pp. A134-A138.

[29] Renganathan, S., Sikha, G., Santhanagopalan, S., 2010, "Theoretical Analysis of Stresses in a Lithium Ion Cell," Journal of the Electrochemical Society, 157(2) pp. A155-A163.

[30] Hu, Y., Zhao, X., and Suo, Z., 2010, "Averting Cracks Caused by Insertion Reaction in Lithium-Ion Batteries," Journal of Materials Research, 25(6) pp. 1007-1010.

[31] Maxisch and Ceder, 2006, "Elastic Properties of Olivine LixFEPO4 from First Principles," Physical Review B 73, 174112.

[32] Woodford, W. H., Chiang, Y., and Carter, W. C., 2010, "Electrochemical Shock' of Intercalation Electrodes: A Fracture Mechanics Analysis," Journal of the Electrochemical Society, 157(10) pp. A1052-A1059.

[33] Agrawal, A., and Carlsson, A. M., 2006, "Obtaining Mode Mixity for a Biomaterial Interface Crack using the Virtual Crack Closure Method," Int J Fract, (141) pp. 75-98.

[34] Sanford, R.J., 2003, "Principles of Fracture Mechanics," Prentice Hall, Upper Saddle River, NJ.

[35] Krueger, R., 2004, "Virtual Crack Closure Technique: History, Approach, and Applications," Applied Mechanics Reviews, 57(2).

[36] Whitcomb, J.D., and Shivakumar, K.N., 1987, "Strain-energy release rate analysis of a laminate with a postbuckled delamination," NASA, 89091, Langley resaerch Center, Hampton, VA.

[37] Wang, L.,Zhou, F.,Meng,Y.S.,Ceder, G., 2007, "First-Principles Study of Surface Properties of LiFePO4: Surface Energy, Structure, Wulff Shape, and Surface Redox Potential," Physical Review B, 76 (165435) pp. 1-11.

[38] Balakrishnan, A., Martin, C. L., Joshi, S. V., 2010, "Effect of Particle Size in Aggregate and Agglomerated Ceramic Powders," Acta Materialia, 58pp. 802-812.

[39] USCAR, United States Council for Automative Research LLC, 2012, "U.S. Advanced Battery Consortium: Energy Storage System Goals".

[40] Francfort, J., 2012, "U.S. Department of Energy's Vehicles Technology Program," Idaho National Lab, SAE Government/Industry Meeting Washington D.C., Jan 2012.

[41] Wang, H., Jang, Y. I., Huang, B., 1999, "TEM Study of Electrochemical Cycling-Induced Damage and Disorder in LiCoO2 Cathodes for Rechargeable Lithium Batteries," Journal of Electrochem Society, 142(2) pp. 473-480.

[42] Krishnaprasad, K., and Prakash, R. V., 2009, "Fatigue Crack Growth Behavior in Dissimilar Metal Weldment of Stainless Steel and Carbon Steel," World Academy of Science, Engineering and Technology, 32.

[43] Borgasano, D., and A123 Systems PR Contact, 2012, " A123 Systems Introduces Breakthrough Lithium Ion Battery Technology that Optimizes Performance in Extreme Temperatures," 2012 (July 10).

[44] EEMB Battery, 2011, "EEMB Designed LiFePO4 Battery with Long Cycle Life," 2012 (July 10).

APPENDICES

Appendix A: ANSYS Project Reports and CINT Results

The following ANSYS report for the L/d=0.3 simulation with CINT results is one of 27 separate reports. Only the L/d=0.3 report will be provided for brevity of the paper, but all CINT results will be listed for the 200nm x 90nm case. CINT is the ANSYS command that executes strain energy release rate and stress intensity factor calculations.

1. Project Report: 200nm x 90nm $LiFeP0_4$

First Saved	Thursday, March 01, 2012
Last Saved	Friday, September 21, 2012
Product Version	13.0 Release

Contents

- Material Data

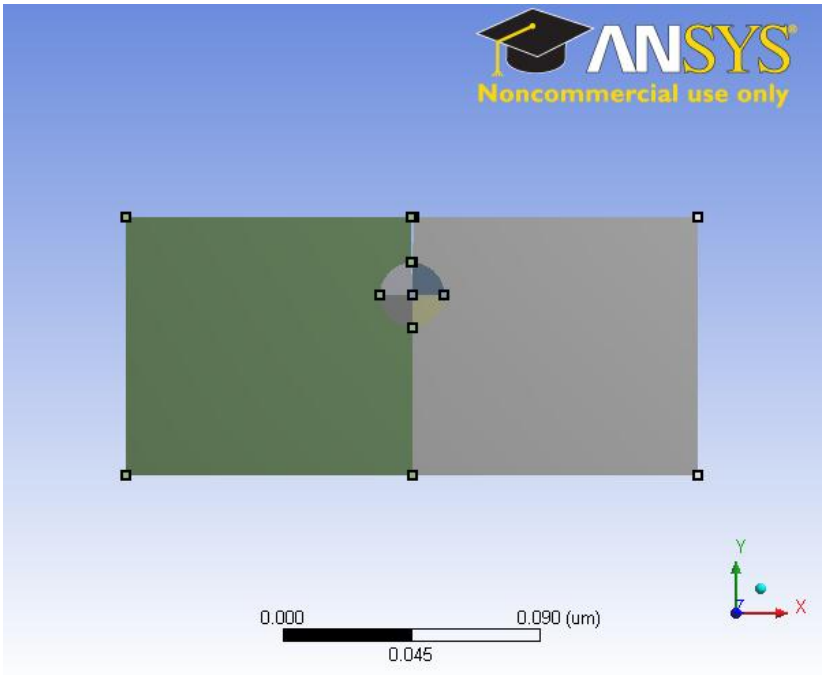

Figure A1. Two-phase material setup with initial crack.

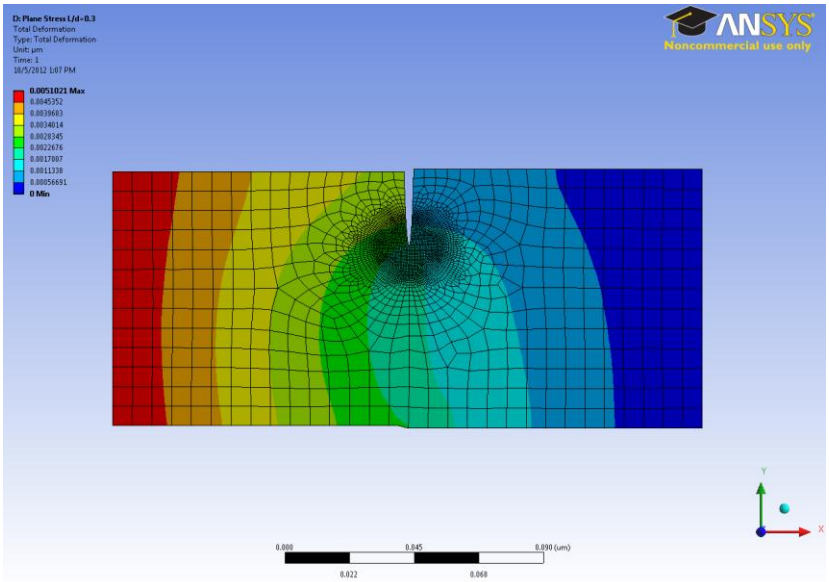

Figure A2. Small deformation (blue=0 um) to large deformation (red=.0051 um).

Units
TABLE A1. Units.

Unit System	Metric (µm, kg, µN, s, V, mA) Degrees rad/s Celsius
Angle	Degrees
Rotational Velocity	rad/s
Temperature	Celsius

Model (D4) Geometry
TABLE A2. Geometry.

Object Name	Geometry
State	Fully Defined
Type	DesignModeler
Length Unit	Micrometers
Element Control	Program Controlled
2D Behavior	Plane Stress
Display Style	Part Color
Bounding Box	
Length X	0.2 µm
Length Y	9.e-002 µm
Properties	
Volume	1.7986e-002 µm³
Mass	6.2863e-017 kg
Surface	1.7986e-002 µm²

Area(approx.)	
Bodies	6
Active Bodies	6
Nodes	10312
Elements	3387
Mesh Metric	None
Preferences	
Parameter Processing	Yes
Personal Parameter Key	DS
CAD Attribute Transfer	No
Named Selection Processing	No
Material Properties Transfer	No
CAD Associativity	Yes
Import Coordinate Syste	No

ms	
Reader Save Part File	No
Import Using Instances	Yes
Do Smart Update	No
Attach File Via Temp File	Yes
Temporary Directory	C:\Users\mastamps\AppData\Roaming\Ansys\v130
Analysis Type	2-D
Enclosure and Symmetry Processing	Yes

TABLE A3. Centroids and moments of inertia I.

Object Name	Part
State	Meshed
Graphics Properties	
Visible	Yes
Definition	
Suppressed	No
Assignment	Multiple Materials

Coordinate System	Default Coordinate System
Bounding Box	
Length X	0.2 µm
Length Y	9.e-002 µm
Properties	
Volume	1.7986e-002 µm³
Mass	6.2863e-017 kg
Centroid X	9.9642e-002 µm
Centroid Y	-4.5027e-002 µm
Centroid Z	0. µm
Moment of Inertia Ip1	4.0131e-020 kg·µm²
Moment of Inertia Ip2	2.0742e-019 kg·µm²
Moment of Inertia Ip3	2.5209e-019 kg·µm²
Surface Area(approx.)	1.7986e-002 µm²
Statistics	
Nodes	10312
Elements	3387
Mesh Metric	None

TABLE A4. Object Assignment II.

Object Name	Surface Body	Surface Bod	Surface Bod	Surface Bod	Surface

		y	y	y	
State	Meshed				
Graphics Properties					
Visible	Yes				
Transparency	1				
Definition					
Suppressed	No				
Stiffness Behavior	Flexible				
Coordinate System	Default Coordinate System				
Reference Temperature	By Environment				
Thickness	1. µm				
Thickness Mode	Refresh on Update				
Material					
Assignment	FePO4	LiFePO4	FePO4	LiFePO4	FePO4
Nonlinear Effects	Yes				
Thermal Strain Effects	Yes				
Bounding Box					
Length X	0.1 µm	1.125e-002 µm			
Length Y	9.e-002 µm	1.1248e-002 µm	1.125e-002 µm		1.1248e-002 µm
Properties					

Volume	8.7966e-003 µm³	9.7744e-005 µm³	9.8898e-005 µm³		9.7744e-005 µm³
Mass	3.0524e-017 kg	3.4406e-019 kg	3.4318e-019 kg	3.4812e-019 kg	3.3917e-019 kg
Centroid X	0.15105 µm	9.5181e-002 µm	0.10476 µm	9.5237e-002 µm	0.10482 µm
Centroid Y	-4.5429e-002 µm	-2.227e-002 µm	-3.1763e-002 µm		-2.227e-002 µm
Centroid Z	0. µm				
Moment of Inertia Ip1	2.0705e-020 kg·µm²	3.8553e-024 kg·µm²	2.1132e-024 kg·µm²	3.9824e-024 kg·µm²	3.8006e-024 kg·µm²
Moment of Inertia Ip2	2.463e-020 kg·µm²	2.1213e-024 kg·µm²	3.9259e-024 kg·µm²	2.1437e-024 kg·µm²	2.0912e-024 kg·µm²
Moment of Inertia Ip3	4.5335e-020 kg·µm²	5.9766e-024 kg·µm²	6.0391e-024 kg·µm²	6.1261e-024 kg·µm²	5.8917e-024 kg·µm²
Surface Area(approx.)	8.7966e-003 µm²	9.7744e-005 µm²	9.8898e-005 µm²		9.7744e-005 µm²
Statistics					
Nodes	2480	1446	1458	1419	
Elements	779	455	459	446	
Mesh Metric	None				

TABLE A5. Centroids and moment of inertia II.

Object Name	Surface Body
State	Meshed
Graphics Properties	
Visible	Yes

Transparency	1
Definition	
Suppressed	No
Stiffness Behavior	Flexible
Coordinate System	Default Coordinate System
Reference Temperature	By Environment
Thickness	1. µm
Thickness Mode	Refresh on Update
Material	
Assignment	LiFePO4
Nonlinear Effects	Yes
Thermal Strain Effects	Yes
Bounding Box	
Length X	0.1 µm
Length Y	9.e-002 µm
Properties	
Volume	8.7966e-003 µm³
Mass	3.0964e-017 kg
Centroid X	4.8951e-002 µm
Centroid Y	-4.5429e-002 µm
Centroid Z	0. µm
Moment of Inertia Ip1	2.1003e-020 kg·µm²
Moment of Inertia Ip2	2.4985e-020 kg·µm²
Moment of Inertia Ip3	4.5988e-020 kg·µm²

Surface Area(approx.)	8.7966e-003 µm²
Statistics	
Nodes	2549
Elements	802
Mesh Metric	None

Coordinate Systems
TABLE A6. Coordinate systems.

Object Name	Global Coordinate System	Coordinate System
State	Fully Defined	
Definition		
Type	Cartesian	
Coordinate System ID	0.	12.
Origin		
Origin X	0. µm	0.1 µm
Origin Y	0. µm	-2.7e-002 µm
Define By		Global Coordinates
Location		Defined
Directional Vectors		
X Axis Data	[1. 0.]	
Y Axis Data	[0. 1.]	
Principal Axis		
Axis		X
Define By		Global X Axis
Orientation About Principal Axis		

Axis		Y
Define By		Default
Transformations		
Base Configuration		Absolute
Transformed Configuration		[0.1 -2.7e-002]

Connections
TABLE A7. Connections.

Object Name	Connections
State	Fully Defined
Auto Detection	
Generate Automatic Connection On Refresh	Yes
Transparency	
Enabled	Yes

Mesh
TABLE A8. Mesh I.

Object Name	Mesh
State	Solved
Defaults	
Physics Preference	Mechanical
Relevance	0
Sizing	
Use Advanced Size Function	On: Curvature
Relevance Center	Coarse
Initial Size Seed	Active Assembly

Smoothing	Medium
Span Angle Center	Coarse
Curvature Normal Angle	Default (30.0 °)
Min Size	Default (1.3688e-003 µm)
Max Face Size	Default (6.844e-003 µm)
Growth Rate	Default
Minimum Edge Length	1.125e-002 µm
Inflation	
Use Automatic Inflation	None
Inflation Option	Smooth Transition
Transition Ratio	0.272
Maximum Layers	2
Growth Rate	1.2
Inflation Algorithm	Pre
View Advanced Options	No
Advanced	
Shape Checking	Standard Mechanical
Element Midside Nodes	Kept
Number of Retries	Default (4)
Extra Retries For Assembly	Yes
Rigid Body Behavior	Dimensionally Reduced
Mesh Morphing	Disabled
Defeaturing	
Use Sheet Thickness for Pinch	No
Pinch Tolerance	Default (1.2319e-003 µm)

Generate Pinch on Refresh	No
Sheet Loop Removal	No
Automatic Mesh Based Defeaturing	On
Defeaturing Tolerance	Default (1.0266e-003 µm)
Statistics	
Nodes	10312
Elements	3387
Mesh Metric	None

TABLE A9. Mesh II.

Object Name	Automatic Method	Face Sizing
State	Fully Defined	
Scope		
Scoping Method	Geometry Selection	
Geometry	2 Bodies	4 Faces
Definition		
Suppressed	No	
Method	Quadrilateral Dominant	
Element Midside Nodes	Use Global Setting	
Free Face Mesh Type	All Quad	
Type		Element Size
Element Size		5.e-004 µm
Behavior		Hard

Named Selections
TABLE A10. Named selections.

Object Name	cracktip
State	Fully Defined
Scope	
Scoping Method	Geometry Selection
Geometry	1 Vertex
Definition	
Send to Solver	Yes
Visible	Yes
Program Controlled Inflation	Exclude
Statistics	
Type	Manual
Total Selection	1 Vertices
Suppressed	0
Hidden	0

Static Structural (D5)
TABLE A11. Simulation type.

Object Name	Static Structural (D5)
State	Solved
Definition	
Physics Type	Structural
Analysis Type	Static Structural
Solver Target	Mechanical APDL
Options	

Environment Temperature	22. °C
Generate Input Only	No

TABLE A12. Analysis settings.

Object Name	Analysis Settings
State	Fully Defined
Step Controls	
Number Of Steps	1.
Current Step Number	1.
Step End Time	1. s
Auto Time Stepping	Program Controlled
Solver Controls	
Solver Type	Program Controlled
Weak Springs	Program Controlled
Large Deflection	Off
Inertia Relief	Off
Restart Controls	
Generate Restart Points	Program Controlled
Retain Files After Full Solve	No
Nonlinear Controls	
Force Convergence	Program Controlled
Moment Convergence	Program Controlled

Displacement Convergence	Program Controlled
Rotation Convergence	Program Controlled
Line Search	Program Controlled
Stabilization	Off
Output Controls	
Calculate Stress	Yes
Calculate Strain	Yes
Calculate Contact	No
Calculate Results At	All Time Points
Analysis Data Management	
Solver Files Directory	C:\Users\mastamps\Documents\1 Research\2012 ANSYS\200x90 ps FINALe_files\dp0\SYS-20\MECH\
Future Analysis	None
Scratch Solver Files Directory	
Save MAPDL db	No
Delete Unneeded Files	Yes
Nonlinear Solution	No
Solver Units	Active System
Solver Unit System	µmks

TABLE A13. Boundary Conditions.

Object Name	Displacement top face -y	Displacement bottom +y	Frictionless Support	Displacement 3
State	Fully Defined			
Scope				
Scoping Method	Geometry Selection			
Geometry	1 Edge		3 Edges	1 Edge
Definition				
Type	Displacement		Frictionless Support	Displacement
Define By	Components			Components
Coordinate System	Global Coordinate System			Global Coordinate System
X Component	Free			-5.03e-003 µm (ramped)
Y Component	-8.55e-004 µm (ramped)	8.55e-004 µm (ramped)		Free
Suppressed	No			

FIGURE A3. Static Structural (D5), Displacement top face –y.

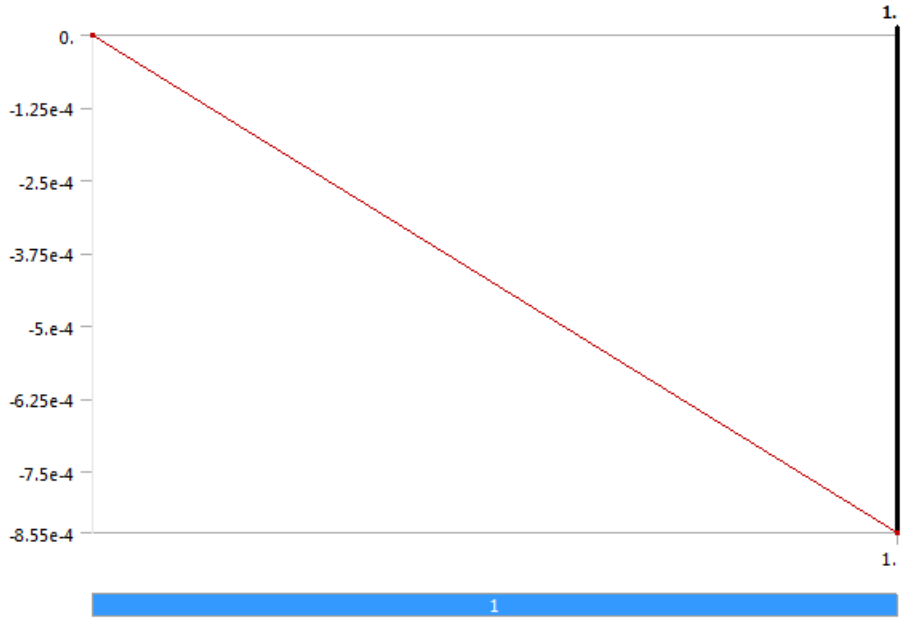

FIGURE A4. Static Structural (D5), Displacement bottom +y.

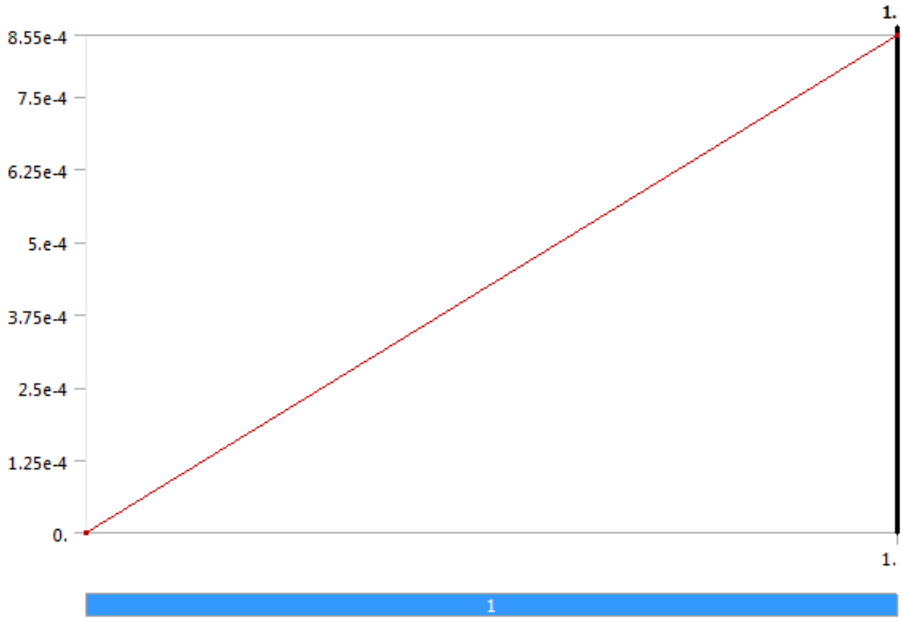

FIGURE A5. Static Structural (D5) > Displacement 3.

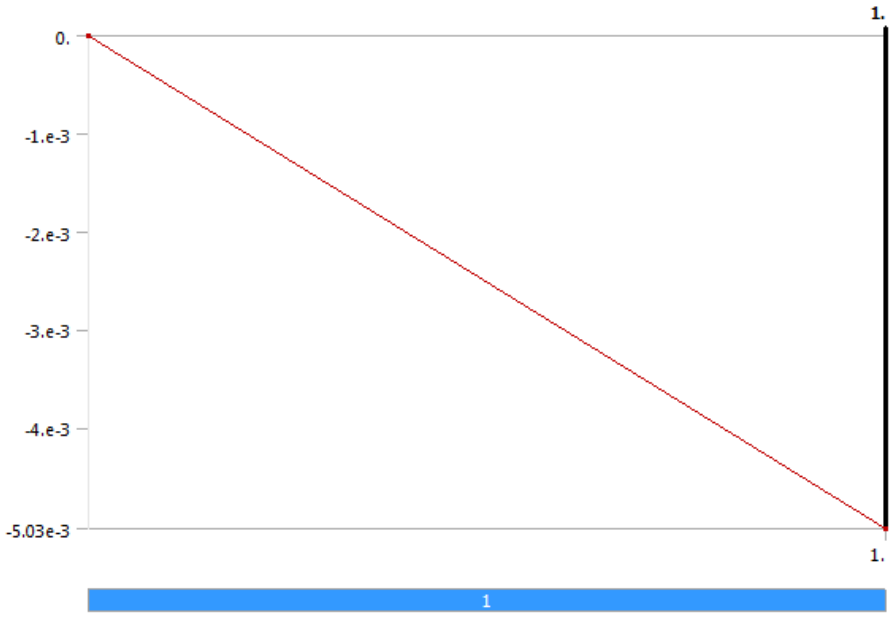

TABLE A14. Static Structural (D5) > Command Snippet.

Object Name	Commands (APDL)
State	Fully Defined
File	
File Name	
File Status	File not found
Definition	
Suppressed	No
Target	Mechanical APDL

Model (D4) > Static Structural (D5) > Commands (APDL)

```
!  Commands inserted into this file will be executed just prior to the Ansys SOLVE
        command.
        !  These commands may supersede command settings set by Workbench.
!  Active UNIT system in Workbench when this object was created:  Metric (um, kg, uN, s,
        V, mA)
cint,new,1
        cint, type, vcct
        cint, ctnc, cracktip
        cint, normal, 12,1
        cint,symm,off
cint,new,2
        cint, type, sifs
        cint, ctnc, cracktip
        cint, normal, 12,1
        cint, ncont, 6
        cint,symm,off
save
        outres,cint,all
fini
        /config,noeldb,0     !       Turn on Element Database
        /solu
```

Solution (D6)

TABLE A15. Static Structural (D5) > Solution

Object Name	Solution (D6)
State	Solved
Adaptive Mesh Refinement	
Max Refinement Loops	1.
Refinement Depth	2.
Information	
Status	Done

TABLE A16. Static Structural (D5) > Solution (D6) > Results

Object Name	Total Deformation	Normal Stress x	Normal Stress y	Shear Stress xy
State	Solved			
Scope				
Scoping Method	Geometry Selection			
Geometry	All Bodies			
Definition				
Type	Total Deformation	Normal Stress		Shear Stress
By	Time			
Display Time	Last			
Calculate Time History	Yes			
Identifier				
Orientation		X Axis	Y Axis	XY Plane
Coordinate System		Global Coordinate System		
Results				
Minimum	0. µm	-5709.8 MPa	-9816.9 MPa	-10670 MPa
Maximum	5.1021e-003 µm	32220 MPa	25678 MPa	19536 MPa
Minimum Occurs On	Surface Body			
Maximum Occurs On	Surface Body			
Information				
Time	1. s			

Load Step	1			
Substep	1			
Iteration Number	1			

TABLE A17. Solution (D6) > Command Snippet

Object Name	Commands (APDL)
State	Solved
File	
File Name	
File Status	File not found
Definition	
Suppressed	No
Output Search Prefix	my_
Target	Mechanical APDL
Input Arguments	

Model (D4) > Static Structural (D5) > Solution (D6) > Commands (APDL)

```
!  Commands inserted into this file will be executed immediately after the Ansys /POST1
       command.
!  Active UNIT system in Workbench when this object was created:  Metric (um, kg, uN, s,
       V, mA)
/show,png
prcint,1
prcint,2,,K1
       prcint,2,all,K2
/show,close
```

Material Data

FePO4

Density	3.47e-015 kg um^-3

TABLE A18. FePO4 Anisotropic Elasticity Inputs.

D[*,1] MPa	D[*,2] MPa	D[*,3] MPa	D[*,4] MPa	D[*,5] MPa	D[*,6] MPa
1.665e+005					
33000	1.277e+005				
57100	9200	1.213e+005			
0	0	0	32500		
0	0	0	0	43000	
0	0	0	0	0	45600

LiFePO4

Density	3.52e-015 kg um^-3

TABLE A19. LiFePO4 Anisotropic Elasticity Inputs.

D[*,1] MPa	D[*,2] MPa	D[*,3] MPa	D[*,4] MPa	D[*,5] MPa	D[*,6] MPa
1.33e+005					
74300	2.03e+005				
54300	55200	1.723e+005			
0	0	0	34900		
0	0	0	0	47800	
0	0	0	0	0	42400

1.1 CINT Results for L/d=0.05

***** POST1 VCCT RESULT LISTING *****
CrackID = 1
Crack Front Node = 711
ENERGY RELEASE RATE Values = -0.65377E-01 0.29928E-02 0.0000 0.68370E-01

***** POST1 K1 RESULT LISTING *****
CrackID = 2
Crack Front Node = 711
Contour Values = 334.78 352.65 350.61 350.78
Contour Values = 356.06 350.15 348.69 343.50
Contour Values = 345.62 354.09

***** POST1 K2 RESULT LISTING *****
CrackID = 2
Crack Front Node = 711
Contour Values = -206.61 -224.46 -228.54 -233.04
Contour Values = -216.24 -145.39 -96.011 -62.598

1.2 CINT Results for L/d=0.1

***** POST1 VCCT RESULT LISTING *****
CrackID = 1
Crack Front Node = 120
ENERGY RELEASE RATE Values = -0.77082E-01 -0.20266E-02 0.0000 0.79109E-01

***** POST1 K1 RESULT LISTING *****
CrackID = 2
Crack Front Node = 120
Contour Values = 489.94 524.15 527.86 529.43
Contour Values = 530.48 531.24

***** POST1 K2 RESULT LISTING *****
CrackID = 2
Crack Front Node = 120
Contour Values = -283.10 -291.28 -291.17 -292.19

1.3 CINT Results for L/d=0.2

***** POST1 VCCT RESULT LISTING *****
CrackID = 1
Crack Front Node = 423
ENERGY RELEASE RATE Values = 3.0880 -0.39256 0.0000 3.4805

***** POST1 K1 RESULT LISTING *****
CrackID = 2
Crack Front Node = 423
Contour Values = 620.78 667.44 671.74 673.07
Contour Values = 673.79 674.16

***** POST1 K2 RESULT LISTING *****
CrackID = 2
Crack Front Node = 423
Contour Values = -198.13 -192.91 -189.19 -187.95
Contour Values = -187.05 -186.45

1.4 CINT Results for L/d=0.3

***** POST1 VCCT RESULT LISTING *****
CrackID = 1
Crack Front Node = 420
ENERGY RELEASE RATE Values = 4.1375 -0.26281 0.0000 4.4003

***** POST1 K1 RESULT LISTING *****
CrackID = 2
Crack Front Node = 420
Contour Values = 718.59 771.56 776.40 777.84
Contour Values = 778.64 779.08

***** POST1 K2 RESULT LISTING *****
CrackID = 2
Crack Front Node = 420
Contour Values = -160.83 -149.41 -144.69 -142.65
Contour Values = -141.24 -140.25

1.5 CINT Results for L/d=0.4

***** POST1 K1 RESULT LISTING *****
CrackID = 2
Crack Front Node = 421
Contour Values = 771.36 827.61 832.70 834.17
Contour Values = 835.01 835.50 835.79 835.93
Contour Values = 835.97 835.89

***** POST1 K2 RESULT LISTING *****
CrackID = 2
Crack Front Node = 421
Contour Values = -129.06 -113.82 -108.77 -106.46
Contour Values = -104.93 -103.88 -103.10 -102.54
Contour Values = -102.13 -101.80

1.6 CINT Results for L/d=0.5

***** POST1 VCCT RESULT LISTING *****
CrackID = 1
Crack Front Node = 428

ENERGY RELEASE RATE Values = 5.0754 -0.10041 0.0000 5.1758

***** POST1 K1 RESULT LISTING *****
CrackID = 2
Crack Front Node = 428
Contour Values = 795.65 853.14 858.27 859.74
Contour Values = 860.59 861.09

***** POST1 K2 RESULT LISTING *****

CrackID = 2
Crack Front Node = 428
Contour Values = -96.910 -79.078 -74.054 -71.717

1.7 CINT Results for L/d=0.6

***** POST1 VCCT RESULT LISTING *****
CrackID = 1
Crack Front Node = 909
ENERGY RELEASE RATE Values = 5.1756 -0.44870E-01 0.0000 5.2204

***** POST1 K1 RESULT LISTING *****
CrackID = 2
Crack Front Node = 909
Contour Values = 839.61 893.17 898.79 900.47
Contour Values = 901.54 902.28

***** POST1 K2 RESULT LISTING *****
CrackID = 2
Crack Front Node = 909
Contour Values = -89.835 -65.060 -60.312 -57.727

1.8 CINT Results for L/d=0.7

***** POST1 VCCT RESULT LISTING *****
CrackID = 1
Crack Front Node = 387
ENERGY RELEASE RATE Values = 7.2407 -0.26336E-01 0.0000 7.2671

***** POST1 K1 RESULT LISTING *****
CrackID = 2
Crack Front Node = 387
Contour Values = 1045.6 1070.2 1069.3 1068.9
Contour Values = 1068.6 1068.4

***** POST1 K2 RESULT LISTING *****
CrackID = 2
Crack Front Node = 387
Contour Values = -84.059 -44.821 -37.756 -32.929
Contour Values = -29.520 -26.880

1.9 CINT Results for L/d=0.8

***** POST1 VCCT RESULT LISTING *****
CrackID = 1
Crack Front Node = 215
ENERGY RELEASE RATE, Values = 5.2939 0.10901E-01 0.0000 5.3048

***** POST1 K1 RESULT LISTING *****
CrackID = 2
Crack Front Node = 215
Contour Values = 865.98 919.79 924.05 925.15
Contour Values = 925.84 926.27

***** POST1 K2 RESULT LISTING *****
CrackID = 2
Crack Front Node = 215
Contour Values = 23.154 51.255 53.798 55.095
Contour Values = 55.327 55.007

Appendix B: MATLAB Iterative Fatigue Cycles Code

1. MATLAB Code: 200nm x 90nm particle

```
%Michael Stamps, 2012 - NC State - Dr. Shadow Huang
% Fatigue Life of LiFePO4 plate-like particle in plane stress
% 200nm x 90nm
% da values are obtained from ANSYS

LD=input('Enter L/d crack length: ');
length=LD*90e-9;
count=1;

while (LD<=1)
 if (LD >=.8)              %start at L/d >=0.8
    count=count+10;
    Cycles_To_Fracture=count;
    Cycles_To_Fracture
    break

 elseif (LD >=.75)          % >=.75
   da=.0589  ;
   dadN=da*10^-9;
   count=count+1;
   length=length+dadN;
   LD=LD+da/90;
 elseif (LD >= .60)           % >=.60
    da=.0591;
    dadN=da*10^-9;
    count=count+1;
    length=length+dadN;
    LD=LD+da/90;
 elseif (LD >= .50)           % >=.50
    da=.0584;
    dadN=da*10^-9;
    count=count+1;
    length=length+dadN;
    LD=LD+da/90;
 elseif  (LD >= .40)          % >=.40
    da=.0535;
    dadN=da*10^-9;
```

```
    count=count+1;
    length=length+dadN;
    LD=LD+da/90;
  elseif (LD >= .30)            % >=.30
    da=.0467;
    dadN=da*10^-9;
    count=count+1;
    length=length+dadN;
    LD=LD+da/90;
  elseif (LD >= .20)            % >=.20
    da=.0327;
    dadN=da*10^-9;
    count=count+1;
    length=length+dadN;
    LD=LD+da/90;
  else                          % L/d smaller than .20
    da=.025;
    dadN=da*10^-9;
    count=count+1;
    length=length+dadN;
    LD=LD+da/90;
  end
end
```

2. MATLAB Code: 500nm x 225nm Particle

```
%Michael Stamps,  2012 - NC State - Dr. Shadow Huang
% Fatigue Life of LiFePO4 plate-like particle in plane stress
% 500nm x 225nm
% da values are obtained from ANSYS

LD=input('Enter L/d crack length: ');
length=LD*90e-9;
count=1;

while (LD<=1)

  if (LD >=.8)              %start at L/d >=0.80
    count=count+10;
    Cycles_To_Fracture=count;
    Cycles_To_Fracture
    break
```

```
elseif (LD >= .60)          % >=.60
   da=.1178;
   dadN=da*10^-9;
   count=count+1;
   length=length+dadN;
   LD=LD+da/90;
elseif  (LD >= .40)         % >=.40
   da=.1675;
   dadN=da*10^-9;
   count=count+1;
   length=length+dadN;
   LD=LD+da/90;
elseif (LD >= .30)          % >=.30
   da=.1471;
   dadN=da*10^-9;
   count=count+1;
   length=length+dadN;
   LD=LD+da/90;
elseif (LD >= .20)          % >=.20
   da=.1125;
   dadN=da*10^-9;
   count=count+1;
   length=length+dadN;
   LD=LD+da/90;
elseif (LD >= .10)          % >=.10
   da=.0697;
   dadN=da*10^-9;
   count=count+1;
   length=length+dadN;
   LD=LD+da/90;
elseif (LD >= .05)          % >=.05
   da=.0628;
   dadN=da*10^-9;
   count=count+1;
   length=length+dadN;
   LD=LD+da/90;
else                        % L/d smaller than .05
   da=.0250;
   dadN=da*10^-9;
   count=count+1;
   length=length+dadN;
   LD=LD+da/90;
```

```
  end
end
```

3. MATLAB Code: 100nm x 45nm Particle

```
% Fatigue Life of LiFePO4 plate-like particle in plane stress
% 100nm x 45nm, x2 surface Es
% da values obtained from ANSYS

LD=input('Enter L/d crack length: ');
length=LD*90e-9;
count=1;

while (LD<=1)
  if (LD >=.8)              %start at L/d >=0.8
     count=count+10;
     Cycles_To_Fracture=count;
     Cycles_To_Fracture
     break
  elseif (LD >= .50)          % >=.50
     da=.0195;
     dadN=da*10^-9;
     count=count+1;
     length=length+dadN;
     LD=LD+da/90;
elseif  (LD >= .35)          % >=.35
     da=.0174;
     dadN=da*10^-9;
     count=count+1;
     length=length+dadN;
     LD=LD+da/90;
  elseif (LD >= .25)          % >=.25
     da=.0133;
     dadN=da*10^-9;
     count=count+1;
     length=length+dadN;
     LD=LD+da/90;
  elseif (LD >= .1)          % >=.10
     da=.0064;
     dadN=da*10^-9;
     count=count+1;
     length=length+dadN;
```

```
    LD=LD+da/90;
  else                    % L/d smaller than .15
    da=.005;
    dadN=da*10^-9;
    count=count+1;
    length=length+dadN;
    LD=LD+da/90;
  end
end
```